Title

Computational Studies of the Influence of Neurodegenerative Damage on Grid Cell Firing Patterns and Navigation

Author

Zhi, Yuduo

Publication Date

2021

Peer reviewed|Thesis/dissertation

Computational Studies of the Influence of Neurodegenerative Damage on Grid Cell Firing Patterns and Navigation

By

YUDUO ZHI

DISSERTATION

Submitted in partial satisfaction of the requirements for the degree of

DOCTOR OF PHILOSOPHY

in

Physics

in the

OFFICE OF GRADUATE STUDIES

of the

UNIVERSITY OF CALIFORNIA

DAVIS

Approved:

Daniel L. Cox, Chair

Rajiv R.P. Singh

Timothy J. Lewis

Committee in Charge

2021

Abstract

Computational Studies of the Influence of Neurodegenerative Damage on Grid Cell Firing Patterns and Navigation

This dissertation consists of two parts: Neurodegenerative damage reduces firing coherence in a continuous attractor model of grid cells, and damage impact on the gird-cell population codes for animal's locations.

The work in Part I is motivated by the discovery of grid cells and their specific grid-like firing pattern: Grid cells, firstly found in the dorsolateral band of the medial entorhinal cortex(dMEC) in 2005, display strikingly regular periodic firing patterns on a lattice of positions in 2-D space. This helps animals to encode relative spatial location without reference to external cues. The dMEC is damaged in the early stages of Alzheimer's Disease, which affects navigation ability of a disease victim, reducing the synaptic density of neurons in the network. Within an established 2-dimensional continuous attractor neural network model of grid cell activity, we introduce neural sheet damage parameterized by radius and by the strength of the synaptic output for neurons in the damaged region. The mean proportionality of the grid field flow rate in the dMEC to the velocity of the model animal is maintained, but there is a broadened distribution of flow rates in the damaged case. This flow rate-to-velocity proportionality is essential to establish coherent grid firing fields for individual grid cells for a roaming animal. When we examine the coherence of the grid cell firing field by studying Bragg Peaks of the Fourier transformed lattice firing field intensity

in both damaged and undamaged regions, we find that for a wide range of damage radius and reduced synaptic strength that for undamaged model grid cells there is an incoherent firing field structure with only a single central peak. In the radius-damage plane this is adjacent to narrow bands of striped lattices (two additional Bragg peaks), which about an orthorhombic pattern (four additional Bragg peaks), that abut the undamaged hexagonal region (six additional Bragg peaks). Within the damaged region, grid cells show no Bragg peaks outside the central one which shows reduced intensity with increasing damage, and outside the damaged region the central Bragg peak strength is largely unaffected. There is a re-entrant region of normal grid firing fields for very large damage area. We anticipate that the modified grid cell behavior can be observed in non-invasive fMRI imaging of the dMEC.

The work in Part II is motivated by a broad goal to explain navigation system: The brain is a remarkable information engine and it's efficiency may come from a hierarchy organization of neurons. At the same time, A unique topographical representation of space is found in the concerted activity of grid cells in the medial entorhinal cortex. Many in this region exhibit a hexagonal firing pattern with grid spacing. And grid spacing has been found to increase along the dorsoventral axis of dMEC but in discrete steps. Such a modular structure provides a new place-coding theory that explains why grid cells has hierarchy organization identified by different spacing. Compared with classical population code (CPC) theory, the hierarchy in grid population code (GPC) improves the coding efficiency and the noise robustness. We developed Sammeet Sreenivasan and Ila Fiete's network model (readout-grid cell network) to construct the GPC process from input signal, through grid cells modules,

to the place cells sensory. The largely stable consistency between input location and inferred location by place cells proves the practicality of readout-grid cell network. Within the completed multiple-layers neural network model of grid coding, we introduce grid layers damage parameterized by radius and by the strength of the synaptic output for neurons in the damaged region. The self-consistence between location signal and inferred location is distributed within reduced coding range. For M layers of the N grid cells, damage within a single layer doesn't destroy the accurate place coding considering the maximum possible coding range ($R \sim N^M$) overloads the reduced coding range ($R_l < 500cm$). We construct the landscape of heat-map showing influence of damage in all situations, and noticed that the layers with bigger spacing (top layers) show more severe disruption given the same condition. This proves the hierarchy theory of GPC that the top panels dominate place coding and fluctuations on big-spacing modules bring more errors.

To

Mom, Dad

my advisor Daniel Cox

and my cats Plum & Walnut

Contents

Illustrations

Figures

Tables

Acknowledgments

We acknowledge useful conversations with M. Zaki Jawaid at the start of the project and with Rishidev Chaudhuri about the origin of flow of the firing peaks with motion.

Chapter 1

Introduction

1.1 Motivation and Background

An accurate representation of animal's position in space is thought to be a fundamental requirement for the brain's navigation system. In 2005, the discovery of grid cells, in the medial entorhinal cortex (dMEC) (Fig. 1.1a), appeared to reveal a much more geometrical, rigid implementation of the cognitive map concept [1, 2]. In small flat environments, these grid cells fire at multiple locations with a regular hexagonal structure (Fig. 1.1b)[1], and, unlike place cells, they fire in all environments regardless of external cues [3]. At the same time, grid spacing increases gradually from the dorsal to the ventral end of entorhinal cortex (Fig. 1.1c)[2], suggesting that the same representation is replicated at multiple scales[5–7]. In the experiment[6], the ratio between successive module spacing averages fluctuated around a constant value of 1.42, indicating that grid scale follows a geometric progression rule (Fig. 1.2b) [3]. It has been proposed that the ratio between adjacent grid scales is $\sqrt{e}$ for idealized neurons and robustly lies in the range 1.4-1.7 for realistic neurons, so that the grid system can minimize the number of neurons required to encode location with a given resolution [8].

---

1. Figure resource from "On the Grid" by Alexis Wnuk.

2. Figure resource: [4]

3. Figure resource: [6]

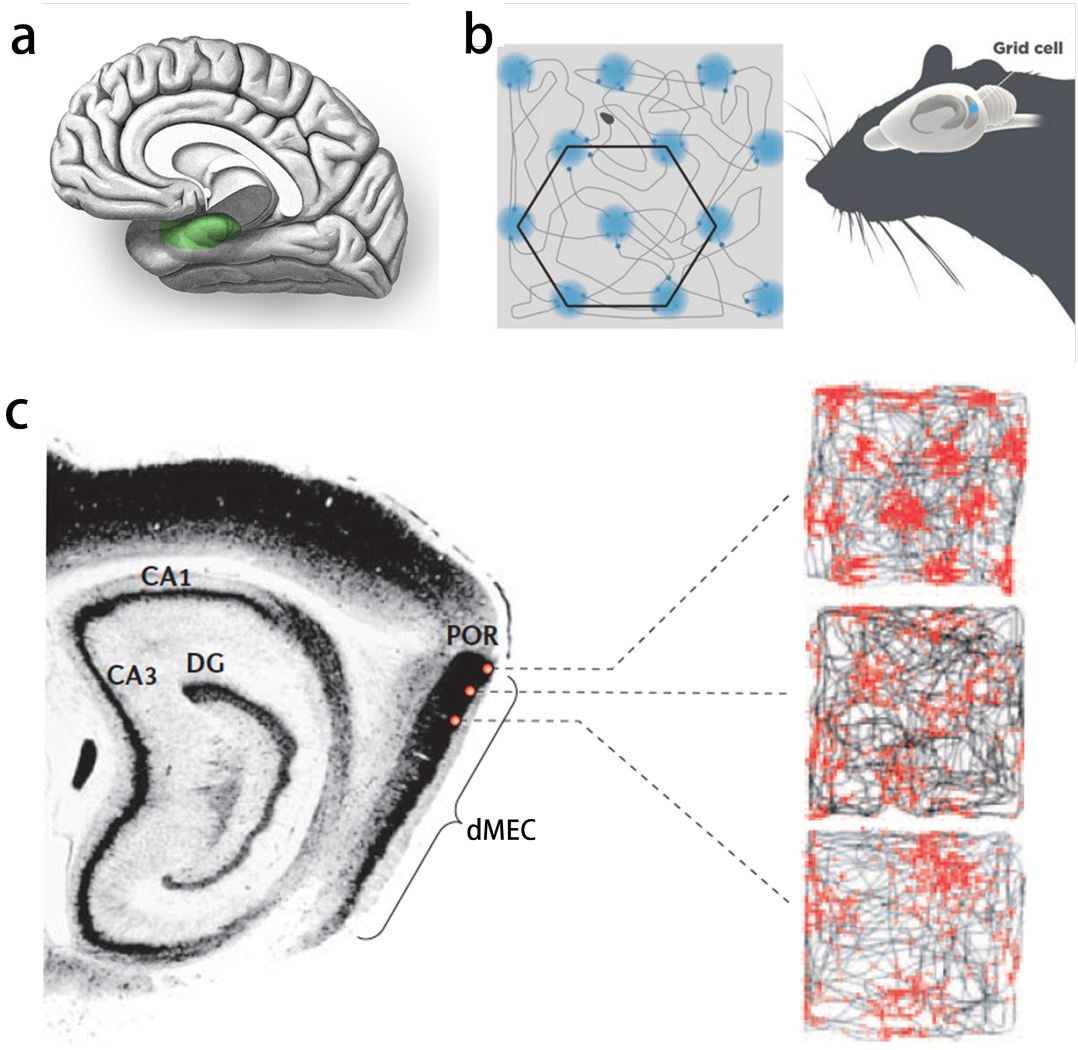

Figure 1.1. **Brain model of dMEC and the discovery of grid cells.** (a) A simplified model of human brain with green region indicating the medial entorhinal cortex (dMEC). (b) Spatial firing map of grid cells. In the experiment, a rat moves in a square enclosure with side length equal to $2m$. Right, blue region is where in space the grid cells fire in rat's brain. Left, rat's trajectory in a square with blue parts representing the location where a rat's grid cells are active. The rat moves for about 15 minutes. A hexagonal lattice firing field is shown in black in the path-integration map.(c) Each panel on the right is the grid firing pattern over the mouse trajectory of one grid cell in dMEC. The locations of emitted spikes are illustrated with red dots, and the paths of the rat as grey lines. The grid scale increases with distance from the border of the dMEC with the postrhinal cortex (POR).

At a given scale, the grid like periodic firing patterns are mainly explained by two competing classes of models: network models based on attractor dynamics [9–11] and oscillatory interference models [12–15]. In this work I will focus on the attractor models only. Yoram Burak and Ila Fiete[10] developed a continuous attractor model that can generate regular triangular grid responses of grid cells, based on inputs that encode only the rat's velocity and direction of movement, and the model successfully achieves an accurate path integration map. Sammeet Sreenivasan and Ila Fiete[16] developed the idea of modular structure of grid cells[7] and constructed a simple neural network that can effectively code accurate locations in 1D space for sufficiently small physical range.

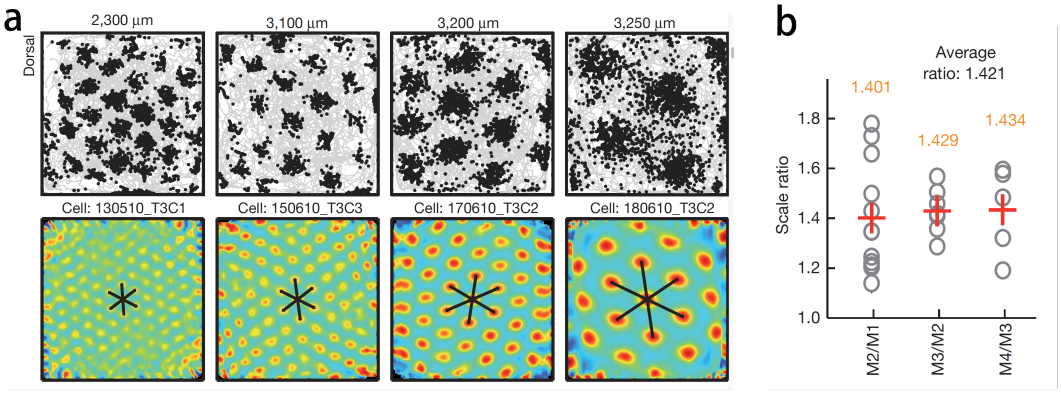

Figure 1.2. **The entorhinal cortex grid map is discretized.** (a) Sample grids at successive dorsoventral positions in a representative 'tangential' animal (rat). Dorsoventral location from brain surface is indicated. Top, neuronal spikes (extracellular action potentials) overlaid on trajectory of rat (grey). Bottom, corresponding colour-coded autocorrelograms with colour scale (-1,1; blue is correlation of -1, red is correlation of 1). Grid spacing was determined from the innermost polygon (black axes). The spatial autocorrelogram reveals repeating activity patterns in the spatial rate map and is generated by correlating the rate map with itself at all spatial offsets. (b) Ratios between successive module means for grid spacing. Individual module pairs in grey, means indicated by red crosses (values in orange). A rough estimation of average wavelength spacing between layers is close to $1.42(\sqrt{2})$.

The surprising geometric behavior of grid cells firing to rat locations has sparked numerous intriguing questions for both experiments and theory: What do grid cells encode? What makes the grid cell code useful for animal's navigation behavior? What kind of neural system can accurately code locations using grid code? To answer above question, we need to consider carefully what are the benefits of using the grid cell code rather than some other coding strategy, and then focus on mechanism: how must the network be wired to generate grid cell responses.

A possible answer is addressed by Fiete[17]: In a 1-d analogue, the population represents the rat position x as a phase within a unit cell of the grid response or modulo remainder of x with respect to the grid period (Fig. 1.3). Because the dMEC contains neural populations with different periods, it is possible to use the phases from different grids to uniquely specify different locations over a much larger range than any of the individual grid periods. The advantage is that grid cell coding capacity grows exponentially with the number of different periods. A highly uncorrelated representation of position at nearby locations can be achieved by grid cell module system.

After the discovery of grid cells, multiple scientists contributed to explain periodic firing pattern generating principle and construct accurate grid coding theory. Building on their work, we turned to think about what is the impact for navigation system when damage happens on grid cells. Considering grid cells in the dMEC display strikingly regular periodic firing patterns on a lattice of positions in 2-D space, and this helps animals to encode relative spatial location without reference to external cues using a completed grid coding scheme. However, the dMEC is damaged in the

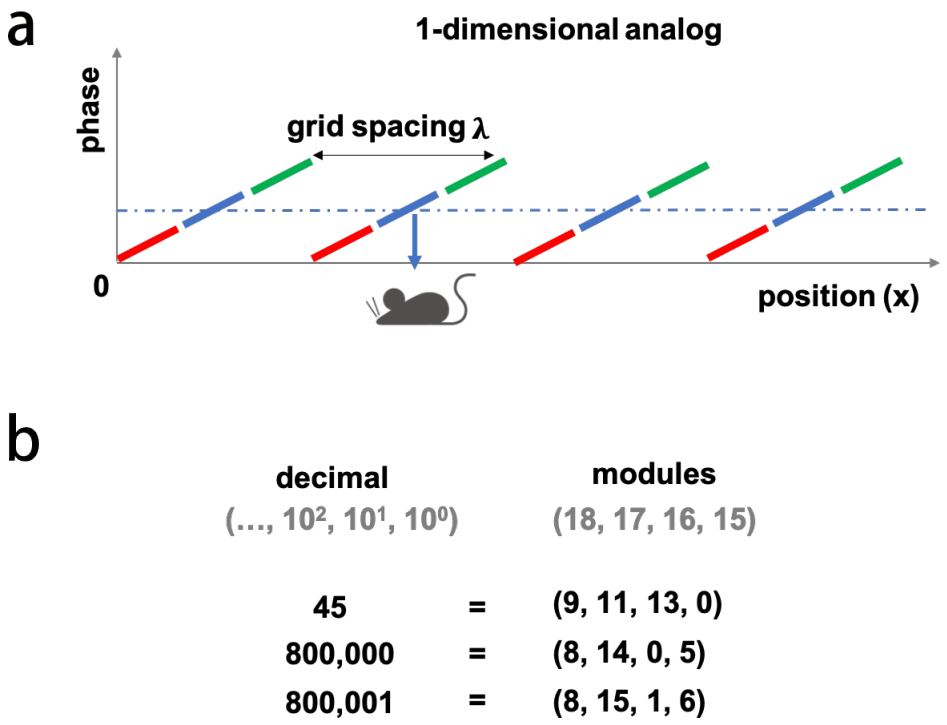

Figure 1.3. **Coding of position by grid cells.** (a) shows the 1D analog of the blue cell fires when the rat is at location x_0 or any location $k \cdot \lambda + x_0$, separated by an integer number k of lattice periods λ. The phase of the blue cells differs from those of the red and green cells. Thus, each grid population represents rat position as the modulo remainder following integer division by the grid period. (b)Left, the position x in decimal, Right, the module system (numbers in grey are the grid periods for each module). The periods can be of similar sizes (for example here) while in face there is ratio between successive modules. All layers are important for representing numbers at all scales: the number 45 and the number 800,000 involve all the layers. When the number 800,000 is incremented by one, all the registers increment; in fact, the module representation is maximally distinct for similar locations, providing a highly decorrelated representation of position at nearby locations.

early stages of Alzheimer's Disease (AD), which affects navigation ability of a disease victim, reducing the synaptic density of neurons in the network. We want to know how the possible damage from AD affects the grid cells and grid coding, describing observable phenomena that those patients suffer the loss of direction/position sense.

In chapter 2, within an established 2-dimensional continuous attractor neural network model of grid cell activity, we introduce neural sheet damage parameterized by radius and by the strength of the synaptic output for neurons in the damaged region. And in chapter 3 we apply the continuous attractor model in the 1D case to reconstruct the grid coding neural network for self-consistent accurate place coding scheme. We firstly rebuild the grid coding neuron networks to verify its efficiency for accurate place coding, and then simulate the central damage model to study its impact. The layers with bigger periodic spacing dominate the place coding and thus they show bigger interference when damage happens compared with smaller spacing modules. We put some prediction and future work in chapter 4, including the astonishing discovery of 3D grid cells for animals that explores a three-dimensional environment like bats [18].

1.2 Objectives and Organization

Motivated by the considerations highlighted in the previous section, the broad objectives of this dissertation are to develop frameworks for the following:

Part I is mainly included in Chapter 2:

(1) Construct Burak & Fiete's attactor model of grid cells in a small 2D space, show that the linear relationship between animal velocity and firing pattern

flow rate is the key to developing the grid cell triangular lattice firing pattern on neuron sheets with that on path-integration map.

(2) Apply mean field analysis to explain triangular lattice grid firing pattern, prove that triangular lattice is the lowest cost compared with other possible periodic lattices.

(3) Develop methods to model the damage derived from synaptic malfunctions on grid cells model, analyze the change on the velocity-flow linear relationship.

(4) Construct Path-Integration Maps starting from grid cells healthy/damaged model, which follow from the flow rate-to-velocity proportionality mentioned in point 1.

(5) Study Bragg Peaks of the Fourier transformed lattice firing field intensity to examine the coherence of the grid cell path-integration maps in both damaged and undamaged regions.

Part II is mainly included in Chapter 3:

(1) Begin with the simplified theoretical model of Sreenivasan and Fiete to compare efficiency of CPC and GPC: In the binary grid coding scheme, N neurons can code N locations in CPC, and can code 2^N locations in GPC.

(2) Improve the binary grid coding to enhanced GPC using readout-grid cell neural network, and verify the effectiveness of accurate GPC location coding.

(3) Construct a damage model for the readout-grid cell neural network. Apply this to model synaptic malfunctions on only grid cell layers without influencing the link between readout cells and grid cells.

(4) Analyze the damage impact on location coding. We introduce error fractions and root-mean-square variation of errors to quantify the behavior of GPC network, and construct a completed damage heat-map diagram over all radius and damage coefficient, to show the board-line between normally functional GPC and disrupted GPC.

Throughout the chapters, we verified the generation of grid-like firing pattern of grid cells path-integration map (using a continuous attactor model) in 2D space. From single layer grid cells to all layers with various periodic spacing, the discrete module structures indicates there may exist an hierarchical architecture of coordinates which can effectively encode animal's immediate location. We achieve an grid code neural scheme following from Ref. [16] that provide a hierarchical organization in the brain's navigation system. The readout-grid network proves its efficiency in simulation experiments and we showed how AD inspired damage to the dMEC affects both the path-integration map and the place coding scheme.

Compared with previous work, we developed the study of damage impact on Bruak & Fiete's continuous attactor model of grid cells; and bind Sreenivasan-Fiete's readout-grid cell network with 1D continuous attractor model of grid cells to construct an enhanced grid population coding (EGPC) scheme. The EGPC makes it possible to consider damage's influence on grid cells place coding and helps to show the hierarchy in grid cell modules.

Chapter 2

Neurodegenerative damage reduces firing coherence in a continuous attractor model of grid cells

2.1 Introduction

There is considerable interest in understanding how the brain encodes location and guides animal navigation. Different neural networks within the brain with various functions help to build animals' navigation system. For instance, place cells in the hippocampus are confirmed to fire strongly at special locations such as reward sites or for the position of external landmarks [19, 20]. Head-direction cells found in many brain areas (e.g., the dorsal presubiculum) [21] fire in 1:1 correspondence with the animal's directional heading with respect to the environment in the horizontal plane [22, 23]. The stunning discovery of grid cells in 2005 showed that these neurons in the dorsocaudal medial entorhinal cortex (dMEC) provide an internal coordinate system encoding absolute position for a given enclosure (longitude and latitude) largely independent of external environmental cues [2, 4]. Each grid cell in a given layer of the dMEC shows enhanced activity (firing) on a periodic hexagonal lattice of points in 2-D space, with the spacing varying with layer depth. Additionally, there is now over a decade of direct evidence that functional Magnetic Resonance Imaging (fMRI) can detect the six-fold symmetry of the grid cell firing pattern noninvasively in healthy brains[24–27]. In this chapter, we do not directly address the question of how neurodegenerative damage affects grid cell based navigation, but we show that the grid

cell pattern can be modified by such damage in a detectable manner that can be observed by non-invasive probes such as fMRI.

Grid cells represent a fascinating example of emergent pattern formation in a nonlinear dynamical system (the coupled neurons of the dMEC). As such, they are of intrinsic interest within the physics of dynamical systems, and amenable to study and characterization by techniques typically reserved for solid state matter, such as diffraction analysis by Fourier transforms (Bragg peaks). How such patterns hold up under perturbation is also of intrinsic interest.

In the case of the dMEC, strong perturbation arises from Alzheimer's disease (AD), which affects the hippocampus (place cells) and entorhinal cortex (grid cells) and thus can disrupt spatial navigation. Several competing hypotheses exist to explain the cause of the disease. The "tau hypothesis", proposes that abnormalities associated with tau protein aggregates initiate the disease cascade [28]. In this model, hyperphosphorylated tau does not hold microtubules together and begins to pair with other threads of tau to form neurofibrillary tangles inside nerve cell bodies [29]. Because the tau protein is what stabilizes the microtubule bundles in neuronal axons on which neurotransmitters and other cargoes relevant for normal synaptic function are transported, this may result first in malfunctions in biochemical communication at the synapses between neurons and later in the death of the cells [30]. Furthermore, the tau tangles that disrupt the axon and synapses may propagate within the brain from location to location, in a manner similar to the prion protein aggregates of mad cow disease [31–33]. In particular, the synaptic output will be degraded by axonal microtubule disruption from tau tangles. The other leading candidates for initiation

of Alzheimer's disease, the "amyloid cascade" hypothesis [34], or the related "amyloid oligomer" hypothesis [35], lead to eventual tau aggregation as well as an end stage.

There is substantial direct evidence for AD related damage to the MEC. Direct post-mortem examination shows significant atrophy of the EC in the brains of AD victims vs. control [36]. fMRI imaging of the MEC region for patients predisposed to early onset AD shows a disruption in the six-fold symmetric firing pattern with respect to the control group when performing virtual navigation tasks, despite no apparent cognitive deficits in the AD disposed group [37]. Similar works on aging adults suggest an impact of AD on the grid cell function and ability to navigate [38]. Amyloid beta oligomers induce tau tangles in cell culture experiments that degrade microtubules and synaptic quality [39]. Overexpression of human tau protein with subsequent aggregation in rats leads to degradation of synaptic plasticity in the MEC and degrades cognitive performance [40], and induced expression of mutant human tau in mice leads to grid cell dysfunction [41]. Finally, there is direct evidence of AD induced synaptic degradation in the neurons projecting from the MEC to the CA1 layer of the hippocampus [42].

2.2 Methods

2.2.1 Emergent Grid-like Firing Pattern in a Continuous Attractor Model of a Neuronal Sheet

In continuous attractor models, each neuron receives inhibitory input from a surrounding ring of local neurons, and the entire network receives broad-field feed-forward excitation containing velocity data from elsewhere in the brain. The model,

upon integration in a static limit, will tend towards a stable fixed point of the coupled equations, i.e., an attractor in the full phase space of the coordinates. When the model animal is moving, given sufficiently rapid response of the neurons in the model, the stable firing pattern can flow in response to the motion and this is the origin of the observed grid cell pattern from this picture. We have based our work upon the continuous attractor model of Burak and Fiete[10], which allows for modest recurrent excitatory synapses between neurons locally surrounded by broadly recurrent inhibitory synapses around a given cell. The model is attractive to use for our purposes here since: (i) it does develop a grid cell like firing pattern in the model sheet, and (ii) with the addition of velocity sensitive response mimicking the input from other parts of the brain (such as from head direction cells) it develops a pattern flow that leads to accurate path integration and a real-space hexagonal firing pattern. However, a purely inhibitory ring is sufficient to obtain grid cells and this is justified by experimental evidence from studies on rats[43]. The mixture of excitatory and inhibitory inputs is an attempt to capture in one model a bipartite entorhinal cortex layer containing both excitatory pyramidal cells and inhibitory interneuron cells.

Consider a network of neurons arranged with uniform density on a cortical sheet(Fig. 2.1a), and with a connection strength that decreases with distance. If the connections of inhibitory cells extend over a wider range than the connections of excitatory cells, it is possible for an emergent symmetry breaking of the firing pattern with a population response consisting of a regular pattern of discrete regions of neural activity to be created, arranged on the vertices of a periodic structure. As analyzed

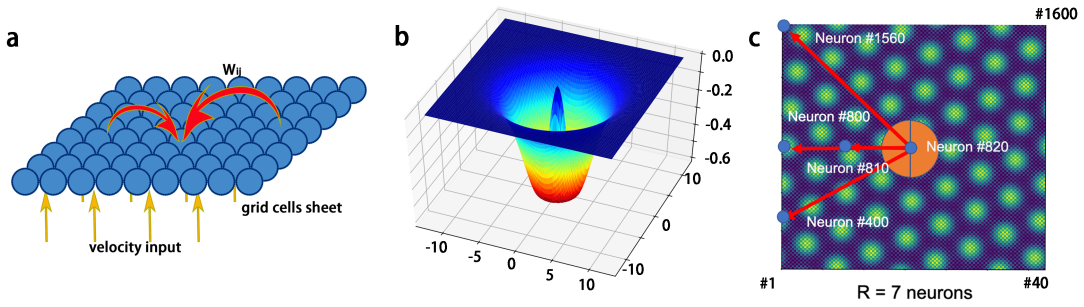

Figure 2.1. **2D neuron sheet and damage model.** (a) Blue spheres are neurons in the grid cell model, and red arrows indicate synaptic connections among neurons, with a weight W_{ij} coupling neuron i and neuron j. The yellow arrows below are the velocity signal from other cells. The instantaneous velocity input is uniform for the grid cell sheet, but each cell has a different preferred direction. (b) The "Mexican Hat" weight matrix W_{ij} is the difference between two Gaussians. It is negative everywhere expect at the center (zero). (c) Central damage model. The heat-map indicates the 40×40 grid cell layer firing peaks, with the orange circle indicating the damaged region (radius $R = 7$ neurons in this case). All neurons are numbered from 1 to 1600, and the neuron at the damage center is #820.

in the appendix A, the most stable steady state structure in undamaged conditions has hexagonal lattice symmetry [19, 20].

The blue spheres in Fig. 2.1a represent grid cells in a 2D neuron sheet, corresponding to one of the grid cell layers of the dMEC. For fast simulation, we use a 40×40 neuron sheet, and the coordinates on that 2D plane can be described by a neuron position vector $\vec{x}_i$.

The dynamics of grid cell activity in this model are described by the coupled differential equations [10, 44]

$$\tau \frac{ds_i}{dt} = -s_i + f(\sum W_{ij} \cdot s_i + B_i) \quad . \tag{2.1}$$

s_i is the i-th neuron's firing rate. τ is the time constant, chosen here to be 10ms, and B_i is the feed-forward velocity input to neuron i (Fig. 2.1a,b), and it introduces

a	λ(neurons)	$\beta(1/\text{neuron}^2)$	$\gamma(1/\text{neuron}^2)$	l(neurons)	τ(ms)	dt(ms)
1	8	$3/\lambda^2$	$6.711 \times \beta$	1	10	0.5

Table 2.1. **Coefficients Table.** λ is the target periodic wavelength of the triangular lattice.

the directional-dependence into model, which is described in detail later. The neural transfer function assumed here, per Burak and Fiete [10], is a simple rectification non-linearity: $f(x) = x$ for $x > 0$ and 0 otherwise. W_{ij} is the synaptic weight from neuron j to neuron i, which has the character that inhibition by neurons operates at longer range than activating ones. Following Burak and Fiete [10], the weight matrix function is written as the difference of two Gaussian curves with different variances which has a "Mexican Hat" shape in position space(Fig. 2.1b):

$$W_{ij} = W_0(\vec{x}_i - \vec{x}_j - l\hat{e}_{\theta_j}) \tag{2.2}$$

with

$$W_0(x) = ae^{-\gamma|x|^2} - e^{-\beta|x|^2} \quad . \tag{2.3}$$

In Eq. 2.2, the neuron separation is shifted by the term $l\hat{e}_{\theta_j}$ per [10]. The neuron preferred direction is $\hat{e}_{\theta_j}$ and we will always choose a non-zero l. This shifted location term plays an important role in driving a statistical flow of the grid cell firing pattern, which is explained in Appendix A in detail.

The weight matrix function $W_0(x)$ in Eq. 2.3 is the difference of two Gaussians: 1) a is chosen to be 1 to make the net response inhibitory, so the value at the center in Fig. 2.1b is zero. A small a is enough to create grid-like firing pattern while $a > 1$

would not affect the result qualitatively. There is a relative excitatory response at small separation compared to the maximum inhibition. 2) β is used to determine the width of the inhibitory response in the surrounding neuron region, and γ sets the shorter distance for the excitatory response in the surrounding neuron region. 3) For the smaller 40×40 system we take $\gamma = 6.711 \times \beta$ to make the maximum inhibition big enough to generate a grid-like firing pattern for a small dimension lattice. The simulation parameters are listed in Table 2.1, in which we have introduced λ, the target periodic wavelength of the formed triangular lattice [10], and we use it to choose β and γ. An approximate relationship is $\lambda \approx \sqrt{3/\beta}$. Using λ made it easier to control the firing pattern lattice spacing and it is explained in Appendix A.

We employ 40×40 neuron sheets to simulate one layer of of the dMEC, but as noted in the introduction we expect a much larger number in the layers of the dMEC, potentially up to a million per layer[45]. The smaller neuronal lattice is chosen purely for computational convenience, and proportional damage compared to the corresponding damage in the full dMEC, i.e., for $R = 10$ so the area is about 300 in model neuronal spacing units, and this would correspond to about 18% of the neurons in a layer being damaged.

All the simulations below are done with zero velocity input, and we start each simulation with small random noise within the range from -0.1 to 0.1 (arbitrary units, but referenced to the static background input of 1), (Fig. 2.2a), then apply the aperiodic boundary condition for a $250ms$ stimulation process. For shorter times, we see randomly separated firing peaks emerge on the inactivated black background (Fig. 2.2b), and the central activity in these peaks is higher than the surroundings.

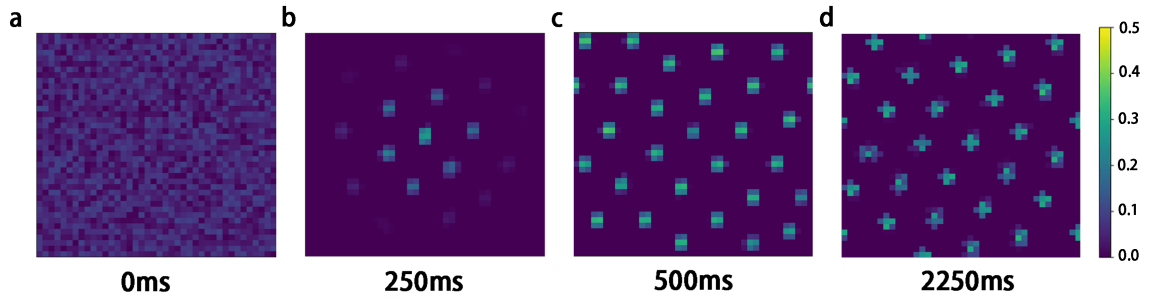

Figure 2.2. **Temporal emergence of firing patterns for undamaged grid cell layer.** (a) Initial state of neuron sheet includes a random noise signal ranging from -0.1 to 0.1. (b) The aperiodic boundary condition shapes the neuronal signal pattern to generate grids in the first 250ms, beginning with an intense central peak with weaker surrounding peaks. (c) Change of the boundary condition from aperiodic to periodic expands the grids evenly. (d) Non-zero velocity inputs ($0.8m/s$ in three directions) heal the defects of previous grids and generate a hexagonal lattice of grid firing peaks. Figures (a)-(d) are heat-maps with the same colorbar.

Then as we run another $250ms$ simulation under periodic boundary conditions, we develop a complete periodic lattice of firing peaks (Fig. 2.2c). The zero velocity input explains why the firing regions are small radius "peaks" instead of the peak clusters (Highlight parts in Fig. 2.2d). Then we let the whole neuron sheet complete building triangular lattice using a annealing process: we apply a nonzero velocity input ($|\vec{v}| = 0.8m/s$) in three directions ($0, \frac{\pi}{5}, \frac{\pi}{2} - \frac{\pi}{5}$), and complete a $500ms$ simulation for each of directions. The annealing process removes the defects and generates a complete triangular lattice (Fig. 2.2d)

2.2.2 Grid-like Firing Pattern Flow

The shifted location term $l\hat{e}_{\theta_j}$ is associated with the neuron's preferred direction $\hat{e}_{\theta_j}$, and these orientation sensitive firings drive the grid pattern from stationary to flowing. This is a way to mimic the input in the model from the head direction

cells. In the head direction system, cells fire selectively with respect to the rat's head orientation as a result of neural integration of head angular velocity signals derived from the vestibular system. In the grid cell system, each neuron receives input from one head-direction cell tuned to its preferred direction, and the neuron's outgoing center-surround connectivity profile is not centered on itself, but is shifted by a few neurons along its preferred direction, which is shown in the weight function above as the shifted location vectors.

In our grid-like sheet, we tiled the neuron uniformly in this way: each neuron i has a preferred direction (W, E, S, N), indicted by $\hat{e}_{\theta_i}$, and each 2×2 neuron block contains all four preferred directions. and then we can define the feed-forward input to neuron i is:

$$B_i(x) = A_i(x)(1 + \eta_0 \cdot \hat{e}_{\theta_i} \cdot \vec{v}) \tag{2.4}$$

where $\vec{v}$ is the velocity of the rat, in units of m/s. η_0 is the coefficient that characterizes the effects of velocity inputs to the driven pattern flow (in Table 2.1). $A_i(x)$ is called the *envelope function* which helps to modulate the strength of the input to the neurons. We assume periodic boundary conditions for firing on the sheet, and in this case

$$A_i(x) = 1 \tag{2.5}$$

We have used neuron sheet of a size 40×40 (1600 neurons) to speed up numerical simulations. And $A_i(x)$ of aperiodic boundary conditions is given in Appendix A.

If we have a non-zero value for the shifted location vector and, then the feed-forward input $\mathbf{B}$ will drive a flow of the formed pattern. η_0 determined the gain of

the velocity response of the network, and the term $\eta_0 \hat{e}_{\theta_j} \vec{v} \ll 1$ stabilizes the flowing lattice. In Appendix A we explain how the feed-forward input drives flow and S3 shows the influence of η_0.

2.2.3 Central Damage Model

As discussed in the introduction, Alzheimer's disease affects the hippocampus (place cells) and the entorhinal cortex (grid cells) early and thus disrupts navigation. It may proceed by diffusion of "tau tangles" from cell to cell which will disrupt synaptic function. We focus on one type of damage to the dMEC that can arise from neurodegenerative diseases and affect grid cell performance: diffusing damage that can arise from propagation of neurofibrillary tau tangles similar to the prion diseases [46]. Based on this model, we model neuronal functional loss as a weakening of the output synaptic strength, which would follow from tau tangle driven disruption and damage to the axonal microtubule bundles. We do not explicitly model tau tangles in the dissertation. As we dial the output strength to zero, we effectively 'kill' the neuron in the model. In Fig. 2.1c, we show a central diffusion damage on top of the grid-like firing pattern. The 40×40 healthy neuron sheets has its own triangular grids of firing pattern, and then the neurons within the orange region are set to be damaged, after which we observe neuron signals in different locations(#820 is within the damage region and #400, 800, 810, 1560 are healthy neurons) and with different sizes of central damage (damage region radius $R = 7$ neurons in Fig. 2.1c).

As the first example (Fig. 2.3a), we kill a central neuron and allow the neuronal damage to propagate outward to model the prion like spread alluded to in the above

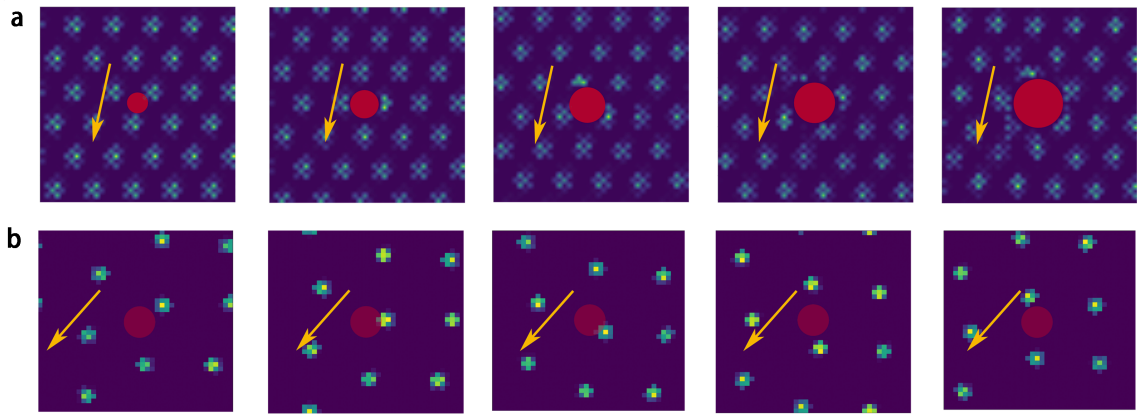

Figure 2.3. **Neuron sheet firing pattern with model damage.** (a) Dead neurons (α=0) in the red damaged regions, with successive damage region radii of 2,4,6,8 neurons. Yellow arrows indicate the flow direction in the opposite direction of the animal velocity, with grid cell firing peaks bypassing the central damage even as it grows. (b) Weakened neuronal firing in the central damage region (red), with $R = 4$ neurons and $\alpha = 0.6$,The whole grid-like firing pattern is moving along the yellow direction, and neurons fire (more weakly) in the damaged region.

paragraph. The time step for numerical integration in our simulation is 0.5 ms and we find that 250 ms total integration time (500 time steps) is sufficient for the surrounding neurons to develop a stable firing pattern. These timescales are obviously significantly accelerated from the AD scale so we can see the effects in a reasonable simulation time frame. The resulting growth speed of the damage cluster radius is 1 neuron/step. We take screenshots every 50 ms to record the damage as we change from a circular damage region with a radius of $R = 2$ neurons to $R = 7$ neurons to see the flow on damaged neuron sheets.

In Fig. 2.3b, we allowed for a nonzero but weakened connection between neurons in the damaged region and to neurons on the periphery of the undamaged region. A new coefficient α is applied to describe the damage: $W_{damage} = \alpha W_{health} (0 \leq \alpha \leq$

1). For those neurons that lie in the circular damaged region (assume neuron i in the damaged area $\mathcal{D}$), their presynapses W_{ji} and postsynapses W_{ij} are not the same anymore, and we assume postsynapses (from damaged neurons to healthy neurons) shall be smaller than presynapses (from healthy neurons to damaged neurons).

$$\begin{cases} W_{ij} = W_{ji} = W_0 \quad (i, j \notin \mathcal{D}) \\ W_{ij} = \alpha W_{ji} = \alpha W_0 \quad (i \in \mathcal{D}, j \notin \mathcal{D}) \\ W_{ij} = W_{ji} = \alpha W_0 \quad (i, j \in \mathcal{D}) \end{cases} \tag{2.6}$$

When two neurons are both healthy, their connection weight W_{ij} and W_{ji} ought to be the same as given in Eq. 2.6; when one neuron is damaged, we assume it can still accept the signal from other neurons with no reduction but that the signal sent from it will be weaker, this is a more realistic assumption of progressive tau tangle damage than simply killing the neuron. We achieved this by multiplying the weights by α for all neuronal outputs emerging from within the damaged region. Note that α=0 corresponds to dead neurons.

2.2.4 Path Integration

Random Walk Generation

A random walk within a circular enclosure is used to simulate the animal's trajectory in real experiments [2]. Here we use the random walk model of Ref. [47].

$$\begin{cases} \vec{v}_{i+1} = \mu\vec{v}_i + \vec{a}_i\Delta t \\ \vec{r}_{i+1} = \vec{r}_i + \vec{v}_i\Delta t \\ \vec{a} \sim \mathcal{N}(0, \sigma_a^2) \end{cases} \tag{2.7}$$

For the ith step, we have velocity $\vec{v}_i$, position $\vec{r}_i$, and acceleration $\vec{a}_i$. The magnitude of the acceleration is drawn from a Gaussian distribution, with average of zero and standard deviation $\sigma_a^2 = 0.5$. The mixing coefficient μ $(= 0.875)$ determines the amount of the current velocity preserved in the next velocity step; this assures a realistically smooth trajectory for which the additional random acceleration boost offers smaller course corrections. We use a small time step $\Delta t = 0.1s$ to make sure the change of the model rat's trajectory is smooth. The velocity is reflected at the boundary, i.e., the component parallel to the boundary is unchanged and the component perpendicular is reversed whenever the model animal would reach the boundary on the next step.

In most situations, the boundary is reached in-between steps ($|\vec{r}_i| < |\vec{R}_{boundary}| < |\vec{r}_{i+1}|$), and thus we recalculate the new position $\vec{r}_{i+1}$ to make it in the reflected direction and have the length $|\vec{r}_i \to \vec{R}_{boundary} \to \vec{r}_{i+1}|$ equal $\vec{v}_i\Delta t$.

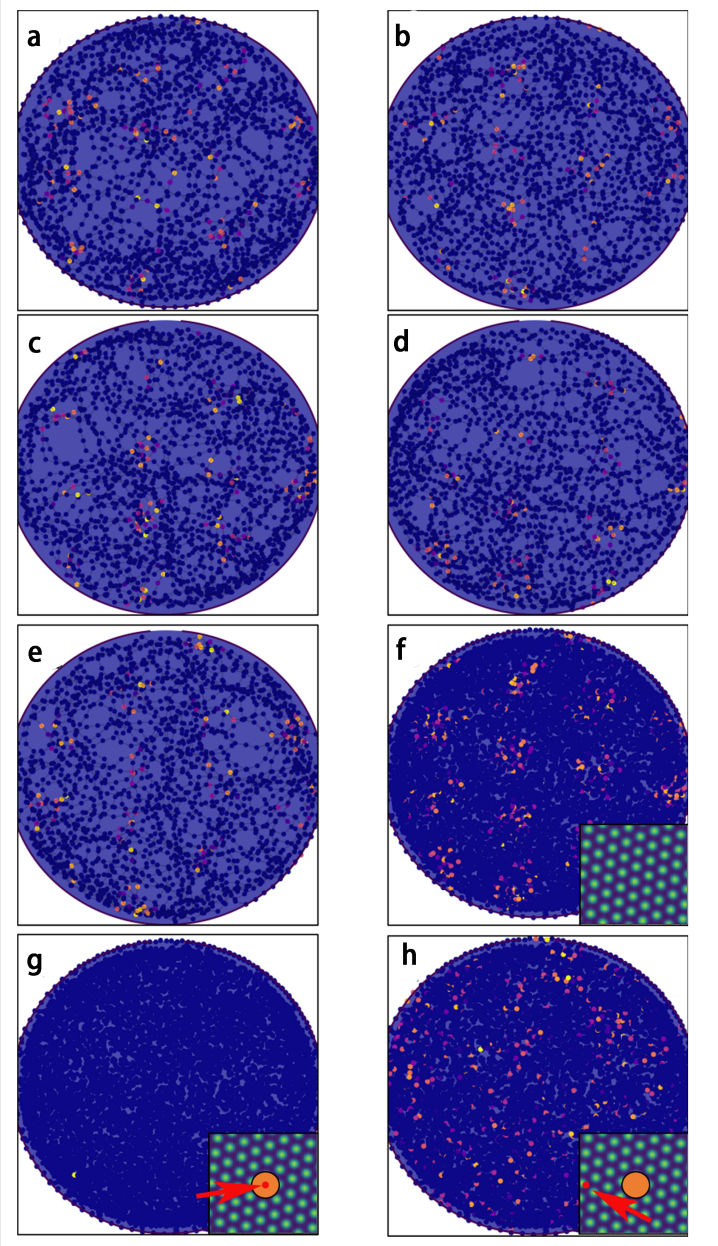

Figure 2.4. **Single path integration map and average path integration maps of healthy/damaged neuron sheets.** (a)∼(e), Single path integration map of healthy neuron sheets for five different trajectories. (f) Average path integration map of the above five shows a clear triangular grid pattern. Inset: grid-like firing pattern in neuron space, 40×40 healthy neuron sheets. (g) The firing of a dead neuron (neuron #820) is muted in path integration map. Inset: grid-like firing pattern in neuron space, 40×40 damaged neuron sheets (orange damage region $R = 7$ neurons,α=0), red arrow points to the tracking neuron's location (within the damaged region). (h) Firing of a healthy neuron (neuron #800) doesn't generate a grid -like average path integration map with damage. Inset: same as (g), but the tracking neuron is outside the damaged region.

Path Integration Map

Now we generate N steps in the random walk path, and each step contains its velocity $\vec{v_i}$ and position $\vec{r_i}$. For each step, the time step $\Delta t = 0.1s$ means updating the neuron sheets' signal 200 times ($0.1s/0.5ms = 200$), and the whole process uses $\vec{v_i}$ as the velocity input to initiative flow in the firing pattern. We track a single neuron for either damaged or undamaged regions and record their firing rates as the model animal moves to the position $\vec{r_i}$. The position and single tracking neuron firing rate are plotted together showing the single path integration map (Fig. 2.4a). This is exactly the same idea of planting electrode measuring activity of a single neuron in a rat's dMEC and tracking the firing signal with the rat's trajectory.[2]

2.3 Result and Discussions

2.3.1 Linear Grid Pattern Flow Velocity Relationship in Healthy/Damaged Models

The dynamics of the firing patterns are associated with the velocity input $\vec{v}$. This velocity changes its direction and magnitude when an animal runs [38], which helps us get the actual path information into our future path integration calculation. With zero velocity input, all the firing peaks will be on vertices of a stationary hexagonal lattice. With nonzero velocity input, the model input with direction sensitive cells tiling the grid cell layer initiates a flow of the firing signal, in the opposite direction to velocity input $\vec{v}$. The linear relationship between the flow speed and velocity input $\vec{\mathbf{v}}$ is very important to generate the later accurate path integration (Fig. 2.4a$\sim$e).

Thus, we introduce the scaling ratio K to describe the relationship:

$$\text{flowing speed} = K \cdot |\vec{\mathbf{v}}| \tag{2.8}$$

For damaged neuron sheets in Fig. 2.3, we observed the whole driving pattern continues, bypassing the damage. The healthy neurons will still fire normally, while the damaged neurons will be fully muted or weaker in excitatory response. The firing pattern of healthy neurons is not strongly influenced by damaged ones, and still shows partial stability with flow. We quantitatively compare the relationship between in healthy neuron sheets and the damaged one in the following.

Fig. 2.5a shows both healthy and damaged neurons sheets retain the linear relationship between average flow speed magnitude and velocity input $\vec{\mathbf{v}}$. Clearly, a damaged neuron cluster with say $R = 7$ is pretty big in our 40×40 neuron sheets, but the proportional relationship between average flow speed and physical speed $\vec{\mathbf{v}}$ is still close to that of the undamaged neuron sheet. The scaling ratio for the healthy one is $K_{healthy} = 26.93\, m^{-1}$ and for damaged one is $K_{damaged} = 25.146\, m^{-1}$.

In Fig. 2.5b, we show the average flow directions under different velocity input directions for both healthy and damaged neuron sheets, and clearly the average flow speed direction remains consistency with the velocity input direction. Note that the damaged one shows a bigger variance at angle $30° \sim 60°$ than the healthy one. In Fig. 2.5c, we increase the central damage region from $R = 0$ to $R = 8$ neurons, and compare the flow speed under the velocity inputs of the same magnitude but different directions $(45°, 90°, 135°)$, The overlap of lines indicates that the change of

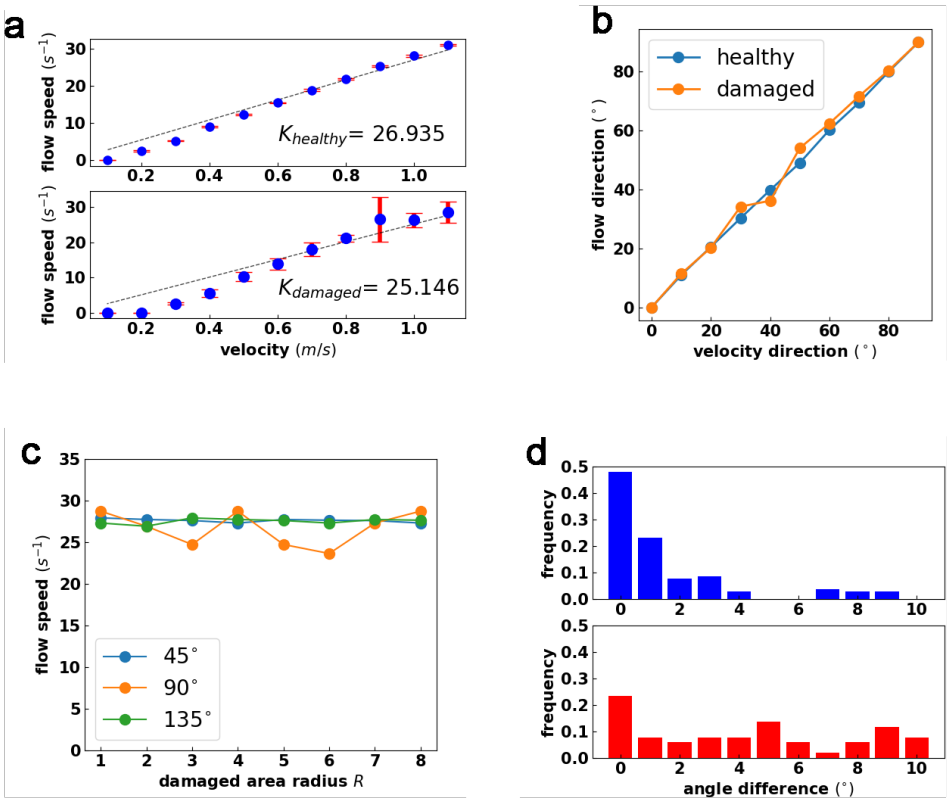

Figure 2.5. **Relationship of firing peak flow speed and velocity input.** (a) Linear relationship of average flow speed and magnitude of velocity input for undamaged cells. Top is in the healthy neuron sheets and bottom is in the damaged neuron sheets ($R = 7, \alpha = 0$), the scaling ratios K are given in the figure, and the error bars are the standard deviation of flow speed data, the dashed lines are fitted line with zero intercept. (b) Stability of linear relationship under different velocity inputs directions. The velocity magnitude is $0.7m/s$, and directions are changed from 0° to 90°. The blue curve is the average flow speed direction in the healthy neuron sheets and the orange one is in the damaged neuron sheets ($R = 7, \alpha = 0$). The direction of average flow speed remains consistent with the direction of velocity input direction.(c) Stability of linear relationship under different damage sizes. The velocity input is $1m/s$ in three directions ($45°, 90°, 135°$), and the central damage size increases from $R = 1$ to $R = 8$ neurons, with the central neurons dead ($\alpha = 0$). The overlapping of horizontal lines indicates the average flow speeds are the same if the velocity input magnitudes are the same, regardless of the change of damage size or velocity direction. (d) Angular difference of flow direction and velocity input direction in both healthy and damaged neuron sheets. Top, healthy neuron sheet, and bottom is in the damaged ones. We recorded the flow direction of 100 firing peaks in both healthy and damaged neuron sheets ($R = 7, \alpha = 0$), and subtract them by velocity input direction 60°. The vertical axis is histogram frequency.

velocity direction doesn't dramatically influence the firing pattern flow, with the same velocity input magnitude ($1m/s$ in Fig. 2.5c). And the increased damaged size along the horizontal axis doesn't change the average flow speed a lot.

Those averaged data show good proportionality between flow rate and velocity in both healthy and damaged neuron sheets, regardless of damage size or velocity inputs (magnitudes and directions). However, when we looked into the detailed behavior, the stability and structural coherence of flow for damaged sheets are poor compared those of healthy sheets. In Fig. 2.5a, the standard deviation (red error bars) of flow speed magnitude in the damaged situation is much bigger than that of healthy ones, meaning the damaged neuron sheets' flow is unstable with fluctuation of flow speed. Then we record the flow direction of 100 firing peaks (peaks are shown in Fig. 2.2d), and subtract them from the velocity input direction (60°). Those 100 firing peaks are divided into 10 groups for different velocity magnitude ($0.1m/s \sim 1.0m/s$) in both healthy and damaged neuron sheets. The good linear proportionality shows in Fig. 2.5b means the average angle difference should be close to zero. Furthermore, we noticed that in the healthy neuron sheets, the stability of the triangular lattice is strong and the angle difference is mostly less than 2°, while in the damaged neuron sheets, the angle difference can up to 10°.

In the damaged neuron sheets, the average flow speed remains proportional to velocity, but there is some deviation between the velocity and flow directions, and in the proportionality of spatial speed and flow speed in damaged neuron sheets which leads to accumulated errors in long-time path integration. This explains why we see the flow pass the damaged region but the path integration map for cells outside the

damaged region cannot generate a triangular lattice (Fig. 2.4h). What is interesting is that we found even in a healthy neuron sheet, that there are still a few firing peaks with big angle differences (Fig. 2.5d top). Those big angle changes in $7^\circ - 9^\circ$ are all from firing peaks with very slow velocity input ($0.1\ m/s$), and it indicates that too small a velocity input inhibits grid stability.

2.3.2 Path Integration Map for the Healthy Neuron Model

From the single path integration simulation, we found the firing pattern shows weak grids, more like discrete highlight dots separated in a grid pattern (Fig. 2.4a$\sim$e). To achieve a more accurate and clear result, we use the average of five different path integration, for each of them, the same tracking neuron signal starts with the same firing pattern at the very beginning, but follows different trajectories. We add the five sets of firing rate together to generate the path integration map. In Fig. 2.4, we can see the average path integration map present better grids pattern compared with single path integration map. The same idea can be applied if we apply a much longer path, like five times longer, however, increasing the length of path will accumulate integration error because the triangular grids still shows fluctuations. And increasing the length costs longer time for a single simulation. The influence of increasing path length is mentioned in Appendix A.

When we replaced the healthy neuron sheet with the damaged neuron sheet model, even though damage does not destroy the signal's average flow stability, it influences the path integration in terms of degrading the triangular lattice firing pattern in the random walk on the two dimensional area. In Fig. 2.4g,h, we found

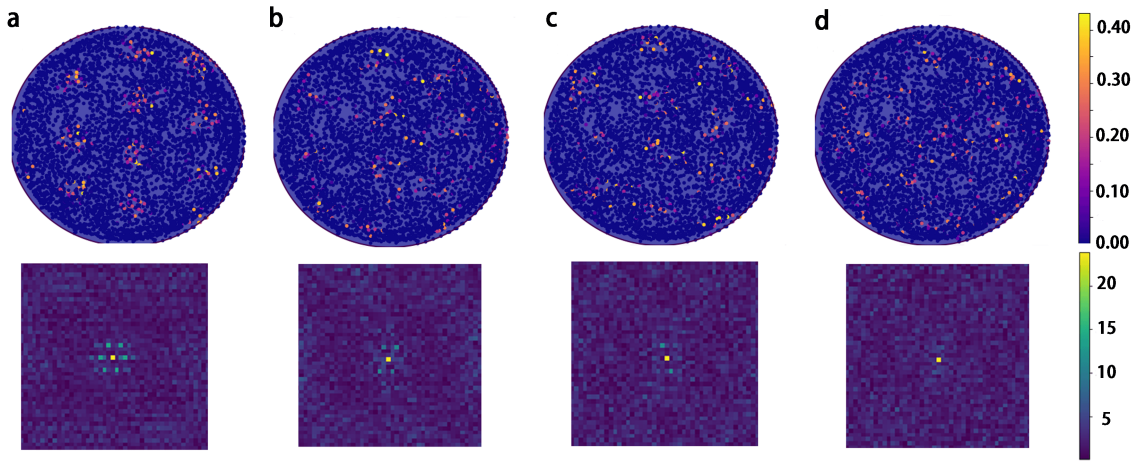

Figure 2.6. **Average path integration map with model damage and discrete Fourier transform (DFT).** (a) For neuron #800, damage coefficient $\alpha = 1$, which is a healthy neuron sheets, the associated average path integration map shows clear triangular grids. DFT diagram has a hexagonal structures of 6 peaks around the center. (b) Neuron #800, damage coefficient $\alpha = 0.5$, damage radius $R = 4$ neurons. DFT diagram has 4 peaks around the center. (c) Neuron #820, damage coefficient $\alpha = 0.3$, damage radius R= 2 neurons. DFT diagram has 2 peaks around the center. (d) Neuron #800, damage coefficient $\alpha = 0.4$, damage radius R= 4 neurons. DFT diagram has 0 peaks around the center. Average path integration maps in (b),(c),(d) are regraded as none-grids path integration map.

the damage from killing neurons brought us the worst influence: even a very small region of dead cells can totally destroy the grid from generating. Tracking the dead neuron in the damaged region (Fig. 2.4g) shows no firing signal all along the path, the healthy neuron outsider the damaged region are strongly influenced by the damage and cannot generate triangular grids like Fig. 2.4f. It seems that the bigger firing pattern fluctuations in damaged neuron sheet accumulate errors in long path. The stability of linear relationship is achieved from single velocity input and not too long simulation ($\sim$ 500ms) while path integration with 1000 steps is about $\sim 100s$.

2.3.3 Fourier Transform Analysis and Damage Phase Diagram

We have found that a small damage region and big damage coefficient α can lead to stable grids, even though too big a damage region size (radius over 7 neurons) or too small a damage coefficient α ($\alpha < 0.2$) still prevent the grids from generating. Fig. 2.1c is a simplified model of 2D 40×40 neuron sheet with central damage $R = 7$ neurons, and tracking neuron #800 is outside the damage region while #820 is within the region. To get a stable input to the Fourier analysis, we crop the center square region of the path integration map to eliminate boundary effects, and do the discrete Fourier Transformation (DFT) on the truncated position space. For those trajectories with clear enough hexagonal grid structure, the DFT diagrams show six Bragg peaks around the center (Fig. 2.6a), where we use the DFT intensity threshold of 15 to quantify the visibility of the peaks to the eye shown in Fig. 2.6 bottom row, and those without grids show only one central peak corresponding to the average firing (Fig. 2.6d). Between these extremes, we find regions with striped firing (2 non-zero Bragg peaks) and orthorhombic firing (4 non zero Bragg peaks anisotropic in the plane) (Fig. 2.6b,c). The application of Bragg peak analysis from the DFT makes it convenient to summarize grid translational and orientational coherence. We want to use the number of Bragg peaks to quantify different levels of grid pattern loses under different damages.

By studying the non-zero Bragg peaks as a function of $1/R$ and α, we can generate the phase diagram shown in Fig. 2.7a,b. The grey area is the no grids region and the blue area is grids region. When α is small, or the damage radius is big

(corresponding to grey area of Fig. 2.7a,b), the loss of a grid like pattern is the worst and there is no Bragg peaks. The opposite is for bigger damage coefficient α or small damage radius R, the grid like pattern remains. What we noticed is that there is a borderline to demarcate the grids and no-grids regions. It means that the grid cells show a tolerance of defects so that they can still work well with damages of certain levels. We find with weak synaptic defects ($\alpha > 0.8$), different sizes of damaged region cannot stop the grid like pattern from generating. And with a poor synaptic connection ($\alpha < 0.5$), if the damage region is not too big ($1/R > 0.5, R < 2$), we can still observe a grid pattern (Fig. 2.7a).

The phase diagrams (Fig. 2.7a,b) of both neurons are similar in detail, but the discrete Fourier Transformation (DFT) central peak intensities varies. Fig. 2.7c is the contour diagram of DFT central peak intensity for neuron within the damage region. The central peak intensity measures the average firing over the space of the 2-D enclosure. The grid cells within the damaged region are not totally muted and also can generate a grid like pattern (in Fig. 2.7b), but its intensity is usually weaker than the grid cells outside the damaged region, and the intensity increases with the distance between the neuron and the damage center.

The phase diagrams of Fig. 2.7 display a re-entrant feature at large damage radius R. The reason this exists is clear from passing to the infinite radius limit. In that case, all neurons have equivalent reduction of their output by the reduction of α, so it is guaranteed that the hexagonal peaks will remain until the peak strength in Fourier space is reduced below its critical value. Hence, the critical α value is determined by the inverse of the peak value of $\tilde{W}(\vec{q})$ For the values of β and γ we use,

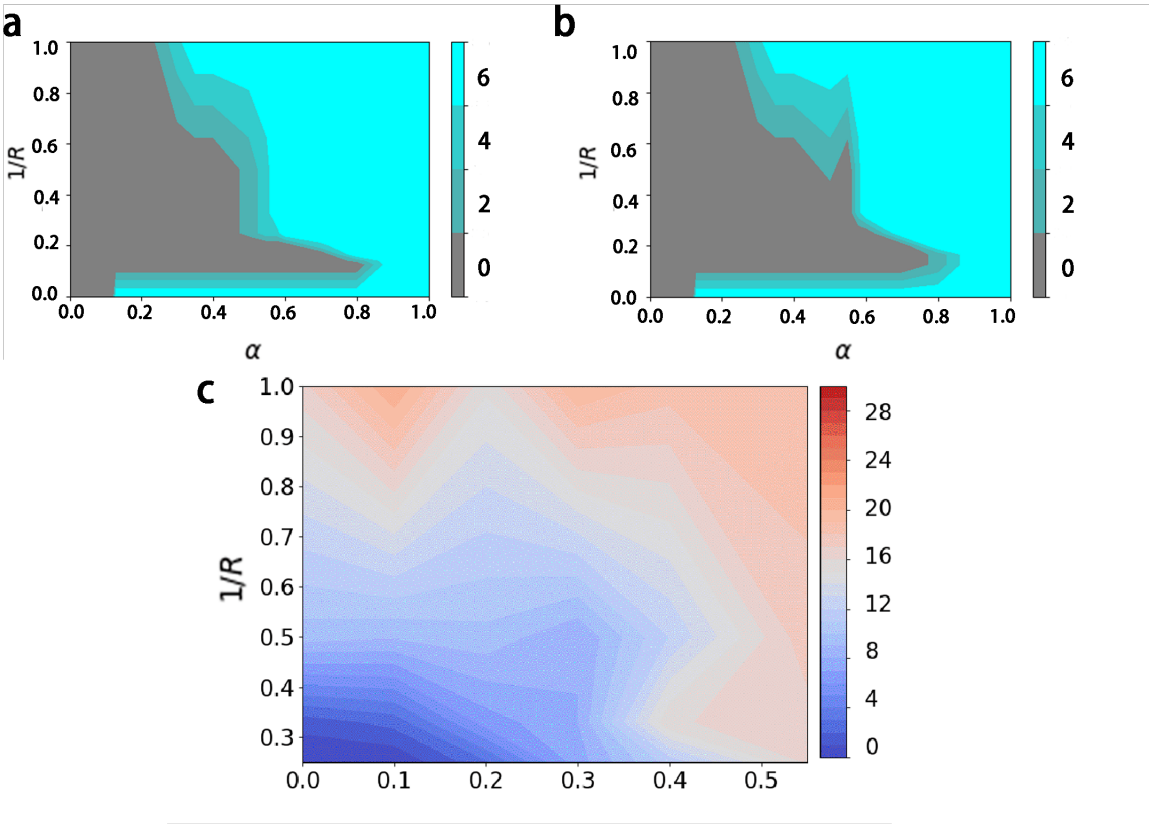

Figure 2.7. **Phase Diagrams and Fourier Transform Central Peak Intensity.** (a) For neuron #800 phase diagrams of grid cell order in the $1/R$-α plane. In the teal region we find hexagonal lattice grids in the average path integration map; in the charcoal region there are no grids in the average path integration map region. The two other shaded regions between teal and charcoal correspond to a striped a grid (2 peaks in the DFT), and an orthorhombic grid (4 peaks in the DFT). For $1/R = 0$, all neurons are damaged α, and for $1/R =$ infinity or $\alpha = 1$ all neurons are healthy. (b) Firing phase diagrams for neuron #820 in the $1/R$- α plane. The structure is nearly the same as the phase diagram in (a). (c) DFT central peak intensity of a neuron (#820) in the damaged region as a function of $1/R$ and α for the phase with no coherent grid structure (charcoal area in (a),(b)).

the analytical estimate for this is, per the Supplemental Information, $\tilde{W}_{max} = 4.37$, which gives $\alpha_c = 0.23$ analytically. The numerical value from 2.7 is somewhat lower ($\alpha_c = 0.14$), but given that the Fourier transform estimate in the Supplemental Information does not include the direction dependent offset necessary for generating flow we are comfortable the argument captures the origins of the re-entrant phase.

As noted in the introduction, while we anticipate that damage will disrupt the coding of position in the grid cell/place cell network, in this chapter we limit our attention to the modification of grid cell symmetry and coherence as a means of providing a map to early detection of neurodegenerative damage.

Chapter 3

Damage impact on the grid-cell population codes for animal's locations

3.1 Introduction

The brain carries out enormously complex information processing operations and uses diverse schemes to encode information. In the area of brain's navigation system, asking what kind of neural network topography can support the sense of place is an interesting question. A hierarchical organization of grid cells may provide an efficient means for place coding [48]. However, in contrast to place cells [49, 50], which encode an animal's instantaneous place by firing only when it is within a neighborhood of a particular location, grid cells fire when animal move on any vertex of a virtual triangular lattice overlaid on the surface of the enclosure. Meanwhile, the entorhinal cortex, where the grid cells are, always plays an important role in spatial memory and navigation. All of the clues suggest that grid cells may be involved in encoding an estimate of an animal's location, but how to associate the spatial periodic grids-like firing pattern of grid cell with the place coding network remains unclear. Fiete[17] proposed modulo remainder method to convert an animal's position x into phases on different grid cell layers ($x \ mod \ \lambda$). This links an animal's trajectory with grid cells firing rate mathematically. Building on the modulo remainder idea, Sreenivasan and Fiete[16] introduced the idea of phase vector for grid population codes and constructed a simple readout-grid cell network that can process place coding/decoding.

In previous chapters, we discussed the grid cells' special firing pattern that may play an important roles in animals' navigation system. The triangular firing pattern of grid cells in a two dimensional neuron sheet can explain the hexagonal lattice of active points in the path-integration map. The lattices seems to be related with animals' navigation system, and the longitude and latitude of the lattice (even the two axes in a hexagonal lattice are not perpendicular with each other) are thought to be used to code the animal's location since it can build us the coordinates[13]. The entorhinal grid cells in mammals fire as a function of animal location, with spatially periodic response patterns, and the entorhinal cortex contains multiple grid layers, with different response periods [2]. We call them as 'grid cell modules', and experiment reveals that each module has its own firing pattern spacing and that there are more than four grid cells modules in rat's dMEC [2, 6, 51]. Those different grid cell modules fire independently given external cues including animals' current location or moving velocity. Binding those firing rates of grid cells in different modules together to code animal's location requires a reasonable neural network. In this chapter, we verify the effectiveness of the Sreenivasan and Fiete readout-grid cell network model when we replace the algebraic grid cell firing rate with real simulation firing rate from continuous attractor Bruak & Fiete's model, and further develop the impacts when damages happen among grid cells.

Population coded[52, 53], obtained from many neurons collectively encoding a given variable, are usually found in sensory, motor and some cognitive areas[22, 54, 55]. Classical population code' (CPC) uses one or several neurons to code one location point, thus CPC requires at least N neurons to code N locations. However,

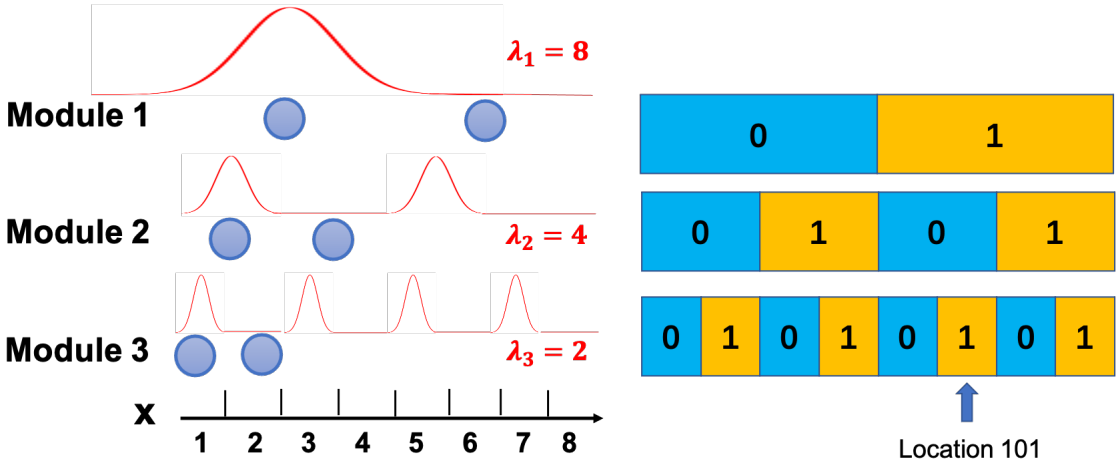

Figure 3.1. **Neuron model of binary grid coding scheme.** (Left) The simplified model contains three one-dimensional modules of grid cells, and the periodic firing pattern wavelength decreases from top to bottom ($\lambda_1 = 8m$, $\lambda_2 = 4m$, $\lambda_3 = 2m$). Bottom is an horizontal axis indicating that the whole coding range is 8m. (Right) Define that left neuron fires (activates) and right neuron mutes to be coding binary bit 1, and the opposite to be binary bit 0. Three layers are matched with three modules of grid cells, and location $x = 6m$ can be represented by binary codes (101).

GPC root mean squared error declines at best as $1/N$ or $1/N^2$ as a function of neuron number N, and the weak accuracy gains with neuron number in CPC are obtained through the inefficient use of neural redundancy. To quantify the efficiency of a redundant code, we define the information rate $\rho \in [0, 1]$ as the ratio of the number of information bits divided by the total number of conveyed bits [56]. In CPC, the mutual information between the code and signal scales as $\sim \log N$. However, the total number of conveyed bits per time step scales as $\sim N$. Thus, the information rate ρ of CPC scales as $\sim \log N/N$, which approaches zero for large N. The grid population codes (GPC) is inspired by the idea that a hierarchical spatial mapping in the brain may improve efficiency of coding position [48], so that a possible hierarchical grid coding scheme may largely outperform the CPC .

Consider the binary grid coding scheme in Fig. 3.1 left where neurons are tuned to respond if the animal is in one of a periodic of array of locations. We have the whole coding range to be $8m$, and the two neurons in the largest module have the period $\lambda_1 = 8m$ and the tuning curve of width $l_1 = 4m$ so that their response just indicates the left $4m$ range or the right $4m$ range. The successive modules have periods $\lambda_2 = 4m$, $\lambda_3 = 2m$. These neuron pairs can successively localize the animal into $1 - m$ bins. For example, if the animal is at the location $x = 6m$, the right neuron in the largest module fires because $x = 6m$ is within the right $4m$ range of the whole, and the left neuron in the second module fires, the right neuron in the third module fires the same way above. If we define that the left neuron firing is bit 0 and the right neuron firing is bit 1 in our binary coding scheme, then a decimal

representing of location $x = 6m$ are changed into binary code (1 0 1) with the largest module at the left side (Fig. 3.1 right).

It is verified that using grid population code (GPC) to explain how the brain effectively codes location grossly outperforms the CPC in several areas: 1) The coding range of GPC grows exponentially with neuron number N; 2) GPC shows extraordinary noise robustness over the reduced coding range; 3) GPC can greatly increase the spatial resolution (difference between the closest two locations). In Fig. 3.1, classical population codes (CPC) need at least 8 neurons to identify all range locations with a spatial resolution $dx = 1m$, while 3 neurons are sufficient to encode all locations in GPC with binary coding. Those 3 neurons shall be lying in 3 modules with different periodicity (wavelength).

In reality, we cannot simplify the grid cell coding to be binary, but experiments[2] proved that the firing pattern of grid cells in different layers shows different wavelengths. In Sreenivasan and Fiete's work [16], they developed an coding scheme using the $x \ mod \ \lambda$ with x to be animal's location divided and λ to be each grid cell layer's spacing (wavelength). In other words, assuming N grid cell layers' with periods $\lambda_1, ..., \lambda_N$, the grid population code is defined as the vector of N spatial phases:

$$\vec{\Phi}(x,t) = (\frac{x \ mod \ \lambda_0}{\lambda_0}, ..., \frac{x \ mod \ \lambda_N}{\lambda_N}) \tag{3.1}$$

with x, t indicates current location of animal. Their theoretical model of GPC successfully construct the coding network. However, there is no theory to explain why the grid cell codes use the 'phase vector'. Furthermore, this model makes it hard to

show what will happen if the grid cells are damaged like that in Alzheimer's disease, considering that we cannot observe above spatial phases of grid cells through experiments and how it changes under damages. What we did different here is to get the firing rate $r(x)$ from simulations using dynamics of grid cells attactor model. Since the grid cell attactor model has been verified by accurate path-integration map in chapter 2, we can get trusted result of firing rate r(x) when animal is at location x.

In chapter 2, we are able to track animal's path integration map using continuous attractor models [10] of grid cells. The path integration map of grid cells shows firing rates when an animal moves within the enclosure; these firing patterns contain the real-time location information x, t. Thus here, we develop an enhanced GPC scheme relative to Ref. [16], employing a one-dimensional model for the grid cell firing rate from continuous attractor model simulations, which leads to emergent periodic firing behavior rather than fixed period oscillatory signals. The enhanced method for GPC shows the same benefits compared with CPC, and it skips the use of the spatial phase vector. We start with an animal's current external information (location, moving time and velocity), and determine the grid cell firing rates in all layers $r_{\alpha,j}(x,t)$ (α module index, j grid cell index in one module). We then sum all the grid cells firing rates together into a readout stage, where model place cells are able to infer the animal's location. Details about the network model are given in the methods section below.

We verified the effectiveness of place coding in this newly-developed GPC network, with a noise-free linear relationship between input location x and inferred location $\hat{x}$ (shown in Fig. 3.7) provided the geographic range is sufficiently small. We

analysed the quality of several different of GPC networks (different coding ranges, grid cells wavelength and numbers, etc.) using the fractional error and the root-mean-square standard deviation of error values (with error defined as the difference between input location x and inferred location $\hat{x}$), and presented their change with increasing coding range for both healthy and damaged cases. Applying the model of damage arising from synaptic degradation among grid cells, we also constructed a complete landscape of GPC network quality heat-map of different levels of damage. The landscape diagram shows the borderline between normal and interrupted networks, and it helps to prove that, in the hierarchical organization for grid cell layers that layers with bigger periodic spacing dominates the place coding.

3.2 Methods

3.2.1 Structure model of EGPC coding network

We use a relatively simple neural network architecture, consisting of grid cells and readout cells. Grid cells are arranged in several layers known as modules, with different layers contains different wavelengths of the periodic firing pattern. The wavelength decreases from the top layer to the one below.

The spatially patterned firing rates of all grid cells across the networks are the inputs to the readout cells. Those grid cells project forward to a readout stage, recurrent global inhibition in the readout stage and symmetric back projections from the readout stage to grid cells.

The connection between grid cells and readout cells are gridcell-to-readout weights W. It is set by Hebbian Learning on the activation of grid cells and readout

cells as the animal runs through a space in the presence of spatially informative external cues. In this run, we assume that grid cell activation is without path integration errors because of the external cues. During this learning process, the readout cells are separately driven to be sparsely active at one preferred location.

After learning, each readout cell is wired to grid cells of all layers, and the gridcell-to-readout weight W is unchanged. When the external cues are absent, grid cells with its activation at different animal's position from its own path integration drive the readout cell. The maximally driven readout cell is identified through winner-take-all dynamics using global inhibition, and its preferred location is the decoded or inferred location.

3.2.2 General algorithm for EGPC

Here we provide a clear description of how the EGPC algorithm works in place coding/decoding (Fig. 3.3). An instantaneous location x is the input, and through its time series it contains information that how fast and how long that animals moves. Grid cells modules are sensitive to those external velocity information and generate corresponding periodic firing patterns. All grid cell firing rate $r_{\alpha j}(x,t)$ are added in a feed-forward fashion to activate readout cells. The summed input $h_i(x)$ in the readout cells vary from each other and we can decode the inferred location by reading the preferred location of the most active readout cell.

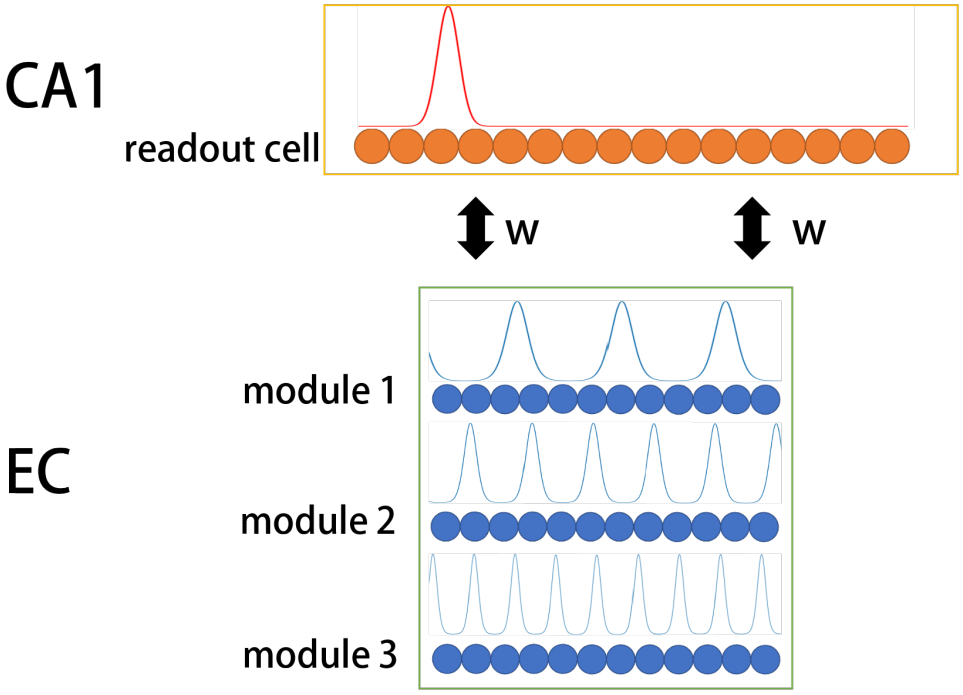

Figure 3.2. **Neuron model of readout-grid cell GPC network.** CA1 of the hippocampus receives direction convergent input from many dorsoventral levels of the entorhinal cortex where the grid cells vary in spatial period. Top box is the readout cells stage in the CA1 and the bottom box is grid cells modules in the entorhinal cortex. Entorhinal-CA1 synapses are indicated using black arrows. The spacing of grid cells periodic firing pattern are decreasing from top module to bottom ones, and the summed input into CA1 are plotted in a red bell-shaped line, showing the right readout cell is activated.

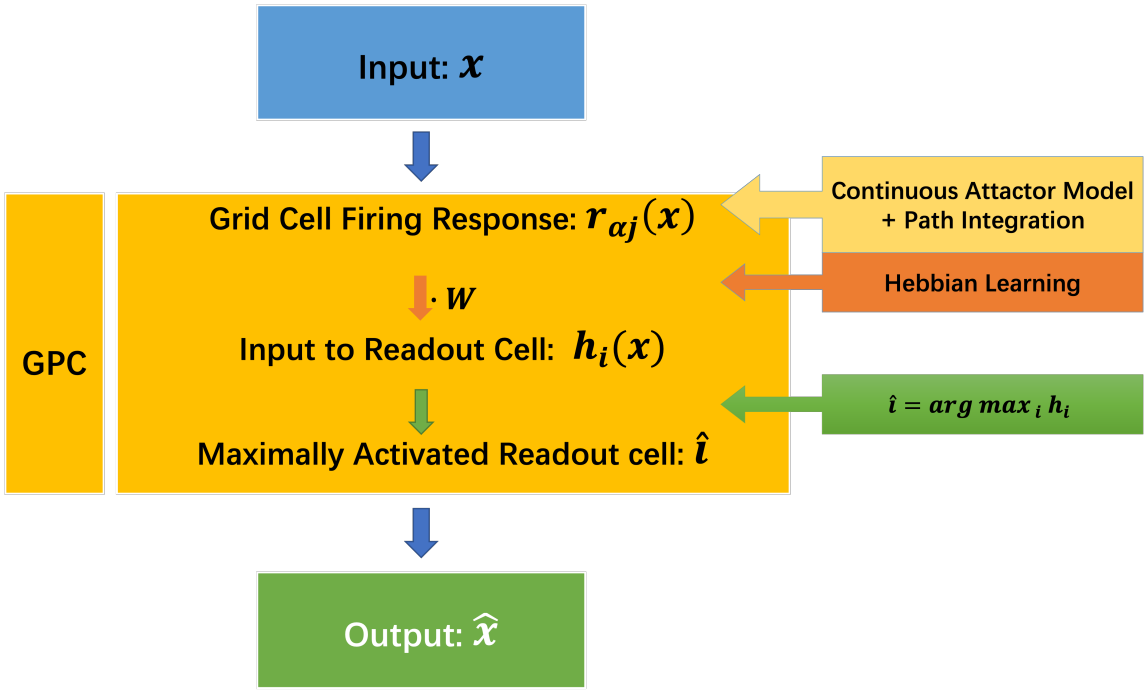

Figure 3.3. **General algorithm of EGPC network.** (top) Input location, (middle) GPC box, including grid cell layers and readout stage, (bottom) Output location/ inferred location decoded by the brain.

3.2.3 Coding range and readout stage

In this 1D GPC decoding model, the coding range is defined as R. It is proved [16] that the length of coding range R influences the noise robustness of GPC or CPC networks: a high-range GPC is pathologically sensitive to noise, and very small noise in the GPC results in massive, nonlocal errors in decoded location.

If the coding range shrinks to a subrange $[0, R_l]$, and R_l satisfy $R_l \ll R$ and $R_l \gg \lambda$, (we use λ to indicate grid cell firing rate spacing), the reduced coding range R_l brings extraordinary noise robustness to GPC network, and it outperformed the CPC network grossly [16]. Thus, when we set the coding range, we don't expect the R_l to be too big.

Given the coding range, we can now define decoding resolution dx to be the minimum position difference that can be distinguished by readout cells, and any two positions with difference less than dx cannot be determined by readout stage. Then the minimum number of readout cells required (indicated as $N_{readout}$) is given as:

$$N_{readout} = \frac{R_l}{dx} \tag{3.2}$$

Each readout cell helps to decode one certain position in the whole coding range R_l, and we call the certain position as readout preferred location ${x_i}^*$, with index i varies from 1 to $N_{readout}$.

3.2.4 Locally peaked response of the readout cells

Given $N_{readout}$ readout cells listed in a single layer as readout stage, we use $r_i(x)$ to present the firing rate of ith readout cell when animal is at location x (unit in cm or m).

Considering that we have required each readout cell has its own special preferred location x_i^*, which means it activates most when animal is at the right preferred location. We have a bell-shaped function $G_\sigma(x-\mu)$ with mean value μ and variance σ^2 to present locally peaked response of the readout cells:

$$r_i(x) = G_\sigma(|x - x_i^*|) = exp(-\frac{|x - x_i^*|^2}{2\sigma^2}) \tag{3.3}$$

the mean value of Eq. 3.3 is at its preferred location x_i^* to satisfy that readout cell activates the most at its right location.

3.2.5 Grid cells arrangement

Grid cells are found to be arranged in several discrete layers or modules (numbers are indicates as N), and with descending wavelengths from the top module to bottom ones. The experimental results indicate that there are about 5∼6 modules of grid cell in mammals' dMEC. For quick simulations, we apply three modules of grid cells and list them in descending wavelengths with a fixed decreasing ratio equal to $\sqrt{2}$, and then we name the top module's wavelength (also called as 'spacing') as $\lambda_{0,cm}$, and cm here means that we measure the wavelength in centimeters.

The three modules of grid cells with their wavelengths are listed below:

$$\begin{aligned} top \quad module: \quad & \lambda_{0,cm} \\ middle \quad module: \quad & \lambda_{1,cm} = \frac{\lambda_{0,cm}}{\sqrt{2}} \simeq \frac{\lambda_{0,cm}}{1.41} \\ bottom \quad module: \quad & \lambda_{2,cm} = \frac{\lambda_{1,cm}}{\sqrt{2}} \simeq \frac{\lambda_{0,cm}}{1.98} \end{aligned} \tag{3.4}$$

Each module contains approximately the same amount of grid cells, indicated as M. A network contains N modules with each module containing M neurons are expected to decode locations accurately up to M^N. This is the outstanding characteristic of GPC decoding network compared with CPC [47]. Thus, for a narrow range of encoding range $R_l < 500cm$ with 500 location points, the number of M only need to satisfy:

$$M > \sqrt[3]{500} \simeq 8 \tag{3.5}$$

We choose $M = 40$, the same as the grid cells setting in chapter 2 (in which there is a 40×40 2D grid cells sheet), and with the same periodic boundary condition that links the head of neurons list with the tail. Following Eq. 3.5, such a 40×3 grid cells network is able to accurately decode up to $40^3 \simeq 64000$ different locations.

3.2.6 Periodic firing rate of grid cells

Different from Sreenivasan and Fiete's method to characterize the firing rate of grid cells using a spatially periodic Gaussian function, we apply the continuous attractor grid cell model of Burak & Fiete, so that we can let grid cells activate corresponding to animal's external location, as the path integration does. The benefit

of the new method for modeling the grid cell firing rate is stated in detail in the discussion part of this chapter. We name the new method "enhanced GPC" (EGPC) compared with the original GPC.

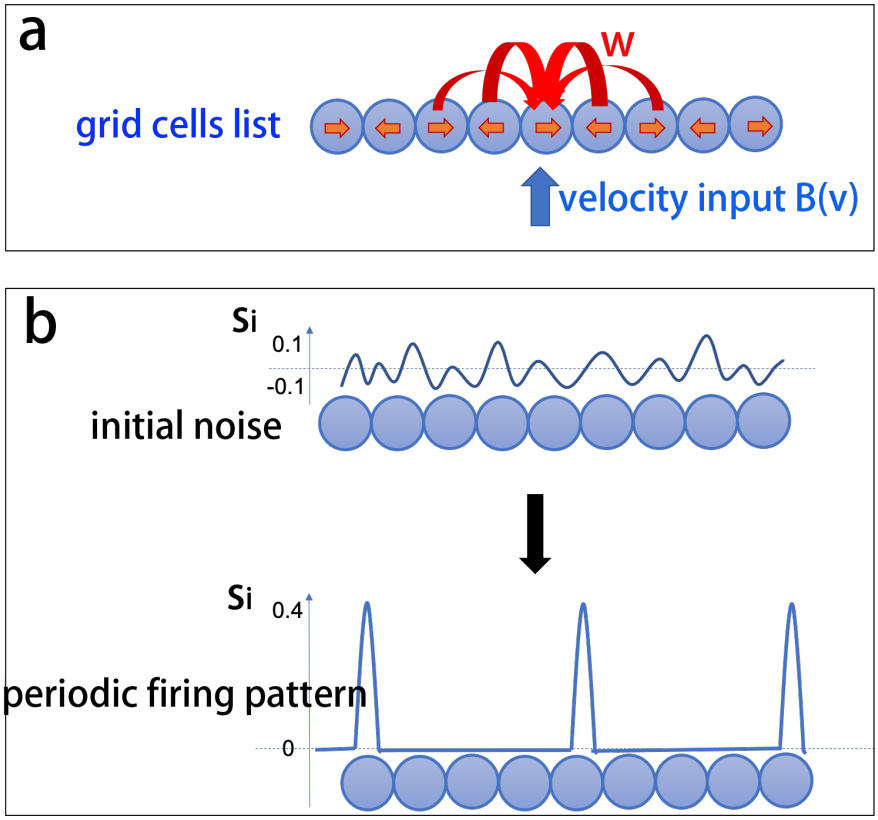

Figure 3.4. **1D continuous attractor model of grid cells.** (a)1D list of spheres represent the arrangement of grid cells, with the orange arrows indicating their preferred directions $l\hat{e}_\theta$, and there are only two directions defined in the one dimensional case, right and left. The grid cell layers receive velocity input $B(v)$ containing animal's moving information. The red arrows are grid cell weights (w) as in Eq. 3.7 3.8. (b) the firing pattern of a grid cell layer; top curve is the initial noise (random number within $-0.1 \sim 0.1$) at the beginning as input, and the bottom shows that the stabilized grid cell firing rate involves periodic pattern with a spatial spacing between two nearby peaks.

We have a list of neurons as the model for one dimensional module of grid cells, and use s_i to present the grid cell firing rate with i to be the index of the list.

We use neuron list of a size 40 to speed up numerical simulations. As in the two dimensional situation in Chapter 2, the dynamics of grid cell activity are described by the coupled differential equations [10, 44]

$$\tau \frac{ds_i}{dt} = -s_i + f(\sum w_{ij} \cdot s_i + B_i) \quad . \tag{3.6}$$

$$w_{ij} = w_0(\vec{x}_i^g - \vec{x}_j^g - l\hat{e}_{\theta_j}) \tag{3.7}$$

$$w_0(x) = ae^{-\gamma|x|^2} - e^{-\beta|x|^2} \quad . \tag{3.8}$$

with s_i, B_i, f to be same definitions as in Chapter 2. To distinguish with the weight matrix W between grid cells and readout cells, we use w to represent the recurrent relationship within the layer of grid cells, and $\vec{x}_i^g$ with subscript ^{g} represents the grid cell's coordinates on a 1D neuron list, different from the real position indication x.

The shifted location term $l\hat{e}_\theta$ plays an important role in driving a statistical flow of the grid cell firing pattern, and we apply the same amount of shift: $l = 1$, but preferred direction $\hat{e}_\theta$ can only be either pointing left or right in 1D case. We define pointing to the right being positive direction, and then Eq. 3.7 obtains a simpler form:

$$w_{ij} = \begin{cases} w_0(\vec{x}_i^g - \vec{x}_j^g - l) & (\hat{e}_{\theta_j}\ to\ the\ right) \\ w_0(\vec{x}_i^g - \vec{x}_j^g + l) & (\hat{e}_{\theta_j}\ to\ the\ left) \end{cases} \tag{3.9}$$

In our 1D neuron list, the neurons with different preferred directions $\hat{e}_\theta$ are tiled uniformly and each 2 neuron block contains all two preferred directions (see Fig. 3.4).

Then we have the feed-forward input to neuron i in the 1D cases given by

$$B_i(x) = \begin{cases} 1 + \eta_0 \vec{v} & (\hat{e}_{\theta_i} \; to \; the \; right) \\ 1 - \eta_0 \vec{v} & (\hat{e}_{\theta_i} \; to \; the \; left) \end{cases} \tag{3.10}$$

where $\vec{v}$ is the velocity of the animal, in units of m/s. η_0 is the coefficient that characterizes the effects of velocity inputs to the driven pattern flow.

We start each simulation with small random noise within the range from -0.1 to 0.1 (arbitrary units, but referenced to the static background input of 1), then apply the aperiodic boundary condition for a $250ms$ stimulation process followed by another $250ms$ simulation under periodic boundary conditions, so that we develop a complete periodic lattice of firing peaks. After that we apply annealing process to cure the defects, using $500ms$ simulation with a nonzero velocity input (0.8 m/s) in right and then left direction.

3.2.7 Firing rate of grid cells at location x

The code/decode network takes the location x as the input, and decode the external cues(like landmarks) as location information inside the brain. What we want to verify here is that given an input location x, the whole GPC network can correctly decode the output location $\hat{x}$ (equal x).

Take a real location x as the input, we would like to know what is the firing rate of each neuron in the network. For grid cells, we use $r_{\alpha j}(x)$ to represent the firing rate of j^{th} neuron on α^{th} module when animal is at location x. The detailed

methods of the simulations of Burak & Fiete's model to get $r_{\alpha j}(x)$ are included in the Appendix B.

3.2.8 Summed inputs to the readout cells

The readout network infers instantaneous location x by finding the maximally activated readout neuron

$$\hat{i} = argmax_i h_i \tag{3.11}$$

where $h_i(x,t)$ are the summed inputs to the readout cells. The operation to identify the maximally driven readout cell is assumed to happen in CA1 through (group) winner-take-all dynamics or other attractor dynamics which produce a narrow distribution of active cells.

The preferred location of the most active cell (marked as $\hat{i}$) is the inferred location

$$\hat{x,t} = x^*_{\hat{i}} \tag{3.12}$$

The summed input h_i to the i^{th} readout cell depends on the firing pattern of the grid cells $r_{\alpha j}(x)$ and on the learned grid cell-readout weights $W_{ij\alpha}$:

$$h_i(x,t) = \sum_{j\alpha} W_{ij\alpha} r_{\alpha j}(x,t) + h_i^0(x,t) \tag{3.13}$$

Here we have h_i^0 represent any non-grid cell input to readout cell i, including input originating from external sensory cues, or input based on predictions or learned contextual priors.

3.2.9 Grid cell-readout weights

The grid cell-readout weights $W_{ij\alpha}$ are set once at the beginning, and we assume they are unchanged after learning. The grid cell-readout weights won't change unless we study the damaged situation of GPC. The learning method is Hebbian learning, within one simulated run over the coding range R_l with noise-free grid cell activation due to external cues and sparse readout cell activation.

$$W_{ij\alpha} = \sum_{x'=0}^{R_l} r_i(x') r_{\alpha j}(x') \tag{3.14}$$

where $r_i(x')$ is from Eq. 3.3 representing the locally peaked response of i^{th} readout cell and $r_{\alpha j}(x')$ is the correct activity pattern of the grid cells for the location x'. Because the learning trajectory is only over the range R_l, readout cells are only activated and assigned preferred locations in that range.

3.2.10 Central damage model on EGPC

As discussed in Chapter 2, we studied the central damage situation on 2D grid cells sheets and its influence on animals' path integration map. The disease we are concerned with, Alzheimer's, may proceed by the diffusion of damage ('tau tangles') among grid cell modules. We consider such damage and its influence on the EGPC decoding networks by assessing the change to the linear relationship between x and $\hat{x}$.

We consider how the synaptic strength within grid cell modules are degraded in this model, and multiply w by a coefficient α, with $0 \leq \alpha \leq 1$, for neurons that lie

within the damage region. In Fig. 3.5, the range of the damage region in one single layer is quantified using radius R, and we center the damage in the middle of the grid cells list. Because the 1D grid cell list with periodic boundary conditions actually is a ring, it doesn't make any difference if we change the center location on the ring.

For the damage coefficient α that changes the connection strength within grid cells, we differentiate the presynapses from the postsynapses in following way: for a grid cell that lies in the damage region, its connection to the outside shall be weaker than the input to itself, in other words, the postsynaptic coupling (from damaged neurons to healthy neurons) is smaller than the presynaptic coupling (from healthy to the damaged neurons). As in the Fig. 3.5, the arrows indicate the weight w, and we define the damage region to be $\mathcal{D}$. For i^{th} neuron within the damage region, we call it $i \in \mathcal{D}$, and j^{th} neuron outside the damage region, $j \notin \mathcal{D}$, the arrow w_{ij} from i^{th} to j^{th} is narrower than w_{ji}, indicating postsynapstic couplings are weaker. Details are given in following equation Eq. 3.15

$$\begin{cases} W_{ij} = W_{ji} = W_0 \quad (i, j \notin \mathcal{D}) \\ W_{ij} = \alpha W_{ji} = \alpha W_0 \quad (i \in \mathcal{D}, j \notin \mathcal{D}) \\ W_{ij} = W_{ji} = \alpha W_0 \quad (i, j \in \mathcal{D}) \end{cases} \tag{3.15}$$

The overall grid cell model contains multiple layers, and the single layer damage defined above can also be applied to multiple layers (Fig. 3.5). For multiple layers, we applied the same damage radius and damage coefficient α, and future work can be done applying different damage parameters in different layers. Here we don't consider

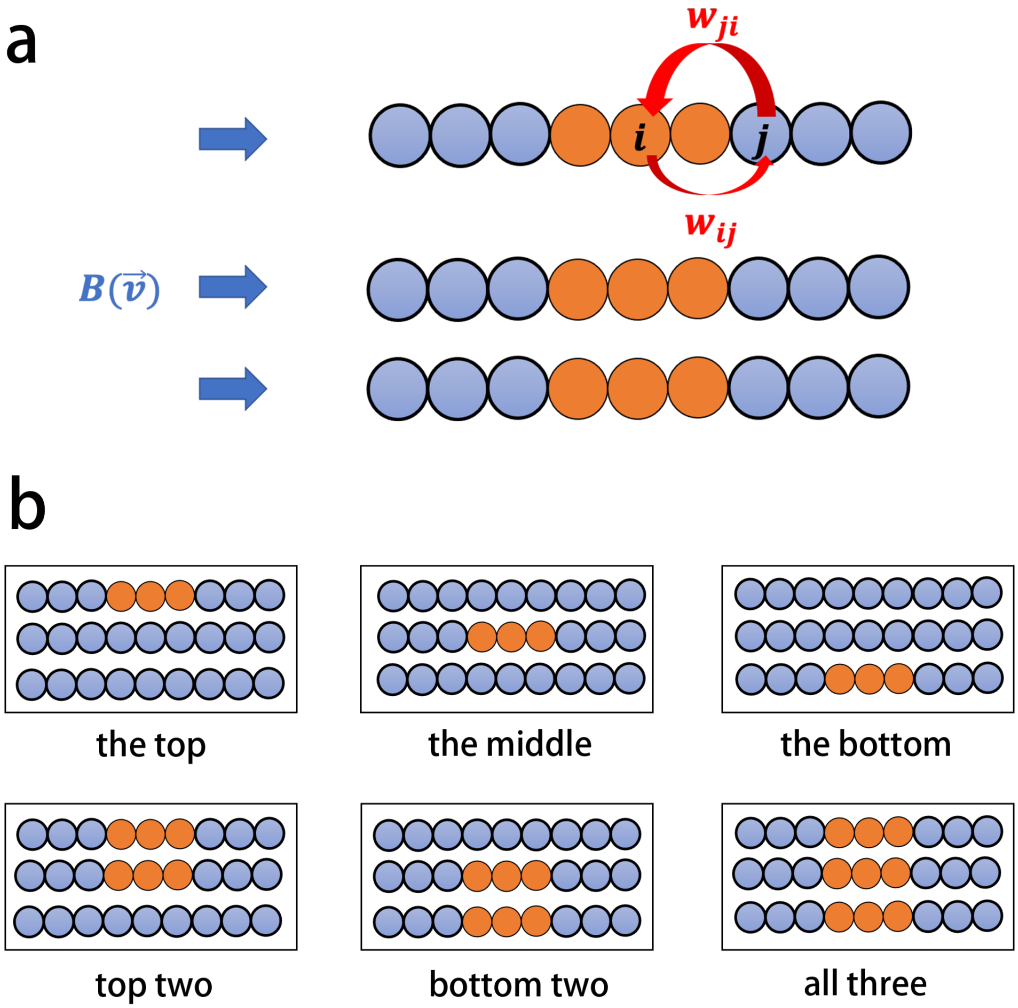

Figure 3.5. **Neural network model of damage to the EGPC network.** (a) Three layers of grid cells with central region to be damaged (in orange, length of damage region equals $2R$). Within the damaged region, weights between neurons are influenced: the connection from j^{th} neuron to i^{th} neuron W_{ij} (the narrow red arrow) is weaker than the connection from i^{th} neuron to j^{th} neuron W_{ji} (the wide red arrow). The whole grid cells part still receive normal velocity input via $B(\vec{v})$. (b) Different arrangement of damage layers. Six possible situations are given as single top layer, middle layer, bottom layer, and top two layers, bottom two layers, and all three layers damaged.

the grid cell connections between different layers, so that with the same velocity input $B(\vec{v})$, each layer of grid cells works independently from other layers.

We assume no damage happens to the connection between grid cells and readout cells, and there is no change on the arrangement of readout cell layer. We summed the firing rates from damaged grid cell modules into the readout stage, as in Eq. 3.13, to encode the new inferred location.

3.3 Discusses and results

3.3.1 Accurate decoding performance of the EGPC

The EGPC decoding can be performed by above simple neural network, and with input location information x put into the grid cell modules, so that the right target place cell on the readout stage can decode the location to be $\hat{x}$. The accuracy of the coding/decoding performance can be shown by the linear relationship of x and $\hat{x}$ (Fig. 3.6a & b). The linear response of EGPC scheme weakens with increasing coding range R_l, when R_l increases to $200cm$, in which errors happens (some inferred locations are shifted from the expected locations) (Fig.3.6c), and more error points are introduced when R_l increased to $400cm$ ((Fig.3.6d)). However, the errors fraction (number of errors divided by total number of location points) among all locations within the range is low and the linear relationship is conspicuous in all given examples in Fig. 3.6.

To track the change in quality of the EGPC linear relationship with different coding range, we applied two characteristics: the fraction of error locations and the root-mean-square of the error (rms), with the error defined as the abso-

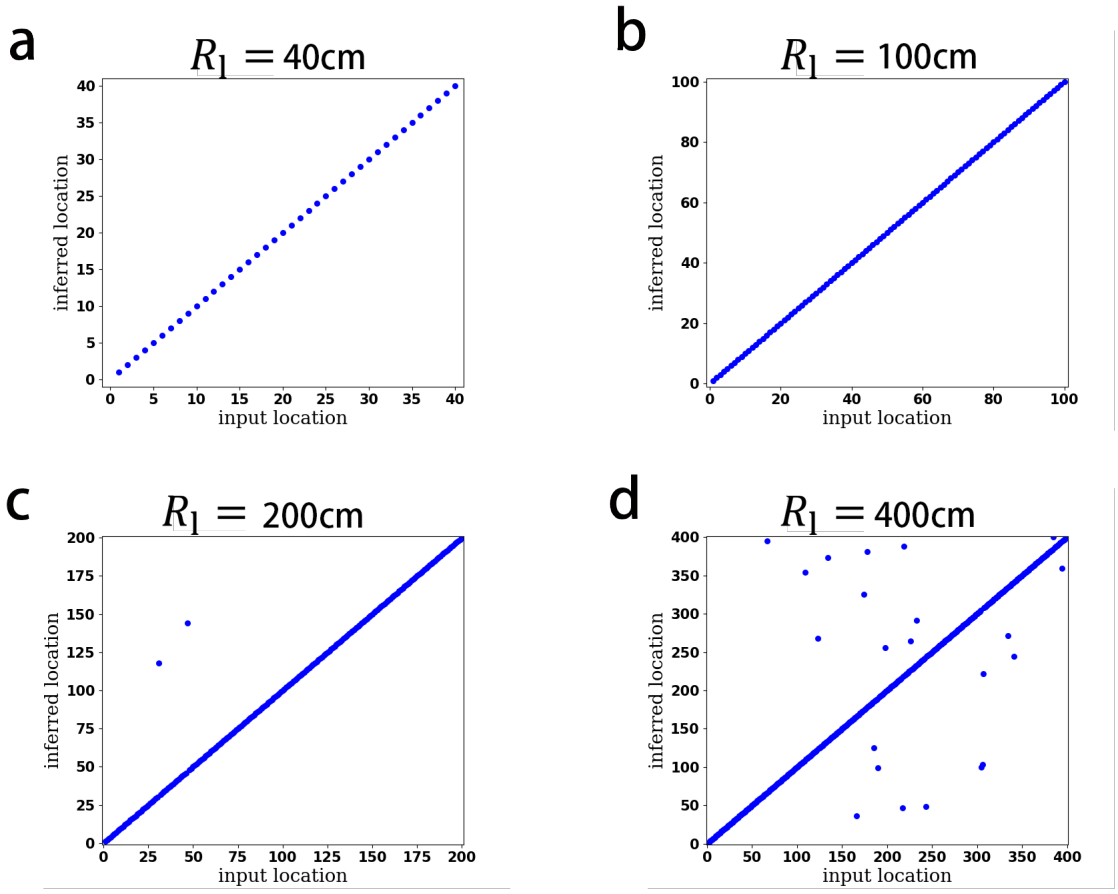

Figure 3.6. **Linear relationship of input location x and inferred location $\hat{x}$ in normal EGPC.** (a) Reduced coding range $R_l = 40cm$. (b) Reduced coding range $R_l = 100cm$. (c) Reduced coding range $R_l = 200cm$. Coding errors occur and two locations are shifted: $N_{error} = 2$ ($x = 31cm \rightarrow \hat{x} = 118cm$), ($x = 47cm \rightarrow \hat{x} = 144cm$). (d) Reduced coding range $R_l = 400cm$. More error location points occur, $N_{error} = 22$.

lute difference between expected location and the experimental location. Here, we have $rms_{R_l=200cm} = 9.21cm$ and $fraction_{R_l=200cm} = 0.01$(Fig. 3.6c); $rms_{R_l=400cm} = 36.98cm$ and $fraction_{R_l=400cm} = 0.055$ (Fig. 3.6d). More figures are given in Fig. 3.7a with the R_l increase from $5cm$ to $500cm$. The rms and errors $fractions$ fluctuate near zero when $R_l < 200cm$, and they increase with increasing R_l above this.

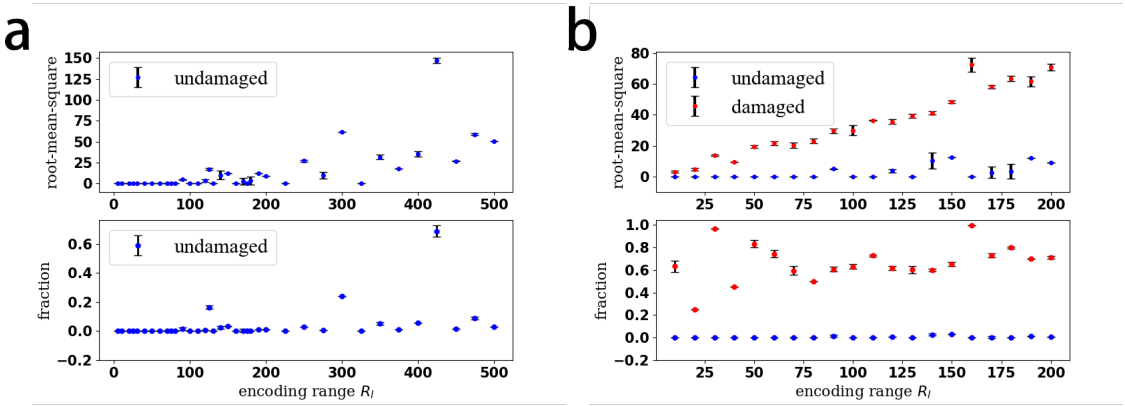

Figure 3.7. **Error fraction and root-mean-square errors in damaged and undamaged EGPC networks.** (a) rms (top) and errors $fractions$ (bottom) in undamaged normal GPC network (500cm): three modules of grid cells and each layer contains N = 40 neurons, step between two nearby location $dx = 1cm$, reduced coding range R_l range from $10cm$ to $500cm$. (b) rms (top) and error $fractions$ (bottom) in undamaged normal GPC network (200cm): three modules of grid cells and each layer contains N = 40 neurons, step between two nearby location $dx = 1cm$, reduced coding range R_l range from $10cm$ to $200cm$. Damage setting: central damage range radius $r = 5$ neurons, synapses weaken coefficient $\alpha = 0.0$. Damage occurs only at the top two layers of grid cell. Error bars are calculated using multiple trials of experiments data and shown in black.

3.3.2 Damage case on grid cells modules

The Error is defined as the absolute difference between correct decoded location and the wrong one. The damaged situation ($R = 5, \alpha = 0.0$, applied on top layers of grid cells modules) are shown in Fig. 3.8, with the same EGPC network setting as

that in section 3.2.3: there are three grid cell layers with wavelength $\lambda_{0,cm} = 99cm$, $\lambda_{1,cm} = 70.21cm$, $\lambda_{2,cm} = 49.79cm$, and each layer contains $N = 40$ neurons for effective simulations. The readout stage contains R_l readout cells (place cells) with decoding resolution $dx = 1cm$, and the reduced coding range from $R_l = 10cm$ to $200cm$. The linear relationship between x and $\hat{x}$ is disrupted in the damaged case, and as shown in Fig. 3.8a, has $N_{errors} = 18$ location points deviated from the correct locations, so we have the error fraction $= \frac{18}{40} = 0.45$, and root-mean-square of error $= 24.07021cm$. Fig. 3.8 shows an increasing tendency of errors when coding range gets bigger, and a more general analysis is shown in Fig. 3.6 b, in which the coding range varies from $10cm$ to $200cm$ with a baseline consisting of data from undamaged situation. Within a reduced coding range $R_l < 200cm$, the undamaged GPC scheme can effectively and accurately codes the animal's location with the maximum rms of errors $12.56cm$ and maximum error fraction 0.39%. In the damaged case, the average rms of errors increases with the coding range and can be up to $72.36cm$ when the coding range is bigger than $160cm$, and the errors fraction is higher above the baseline with a minimum of 25% and a maximum of 96%.

For all possible situations including single layer damage, two layers damaged and all three layers damaged, we studied different levels of damage: from the weakest ($\alpha \sim 1.0$) to the killing neuron ($\alpha = 0$), and the radius are changed within no damage ($R = 0$) and whole layer diminished ($R = 20$). All results are presented in Fig. 3.9.

Root mean square (rms) of errors are plotted with variable radius R and coefficient α in Fig. 3.9a, and another characteristic error fraction is shown in Fig. 3.9b. Those two heat-maps are consistent with each other, showing that the damage case

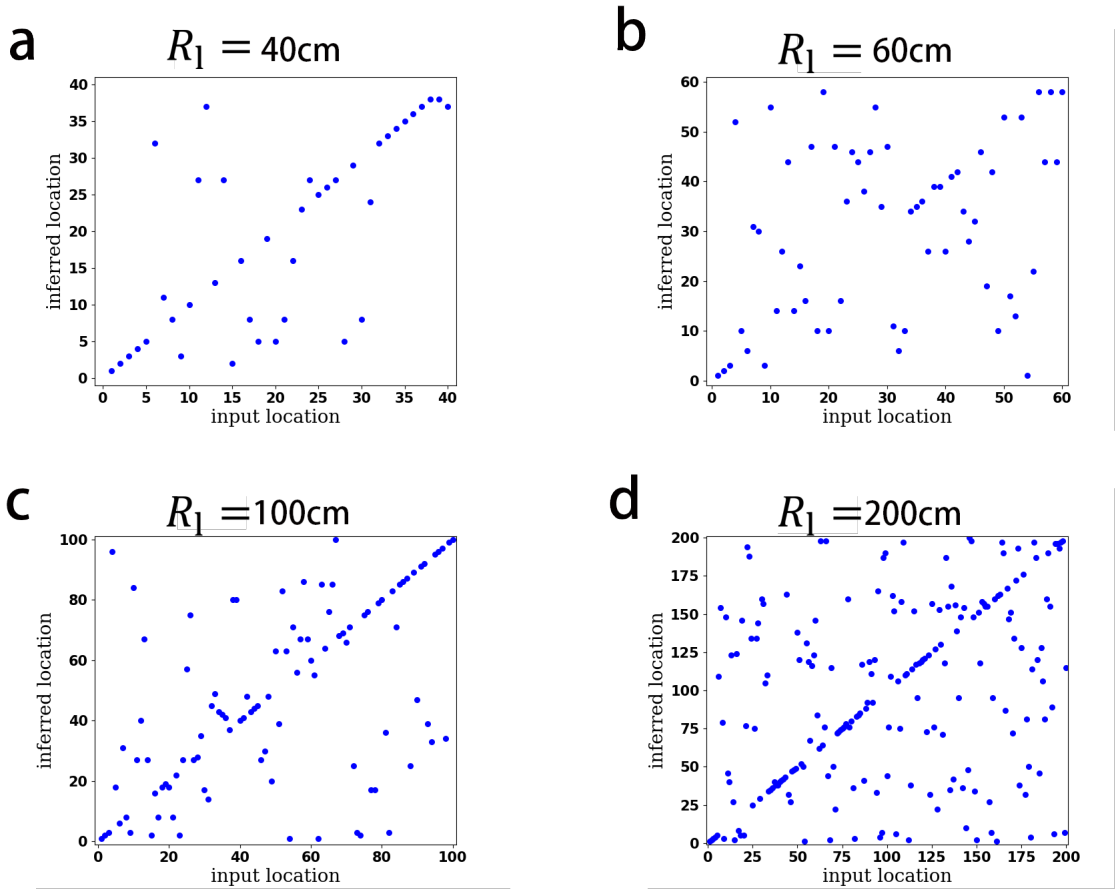

Figure 3.8. **Interrupted linear relationship of input location x and inferred location $\hat{x}$ in damaged GPC.** (a) Reduced coding range $R_l = 40cm$. $N_{error} = 18$. (b) Reduced coding range $R_l = 60cm$. $N_{error} = 45$. (c) Reduced coding range $R_l = 100cm$. $N_{error} = 60$. (d) Reduced coding range $R_l = 200cm$. More error location points occur, $N_{error} = 144$. (Damage: $R = 5, \alpha = 0.0$, applied on top layers of grid cells modules).

with bigger error fractions comes with bigger root mean square of errors at the same time. We can observe the borderline between the blue region and the grey region (with grey indicates interrupted case), and the borderlines are also self-consistent in Fig. 3.9a and b, except the error fraction boundary gets fuzzy in single layer cases. Most regions in top panels of the Fig. 3.9a and b are colored blue, showing that the damage on one single layer out of three can still allow robust function for place coding.

A more general behavior among all six cases is that a narrow blue region shows up when the damage coefficient is close to 1.0, or the radius is very small ($R < 2$ neurons), which agrees with expected result that small size of damage or weak damage doesn't influence the EGPC network severely. The increasing color shade of the grey from top to bottom panels shows that increasing the number of damage layers brings more severe disruption.

What's interesting is the variety of behaviors that arise within the single layer cases (or two layer cases). In the top panels of Fig. 3.9a, we observed that the landscape in middle layer and top layer fluctuates much more than the bottom layer. Root mean squares are higher than that in bottom layer case even the error fraction plottings are similar. In the bottom panels, top two layers case is more severe than bottom two layers. The variation within the same damage layer situations show that the same damage leads to different effects on different layers, and it turns out that the damage on the layer with bigger grid spacing exerts more influence on the EGPC decoding. It is consistent with the previous motivation of GPC (Fig. 3.1), where we stressed that the grid layer with bigger spacing dominates the place coding. The

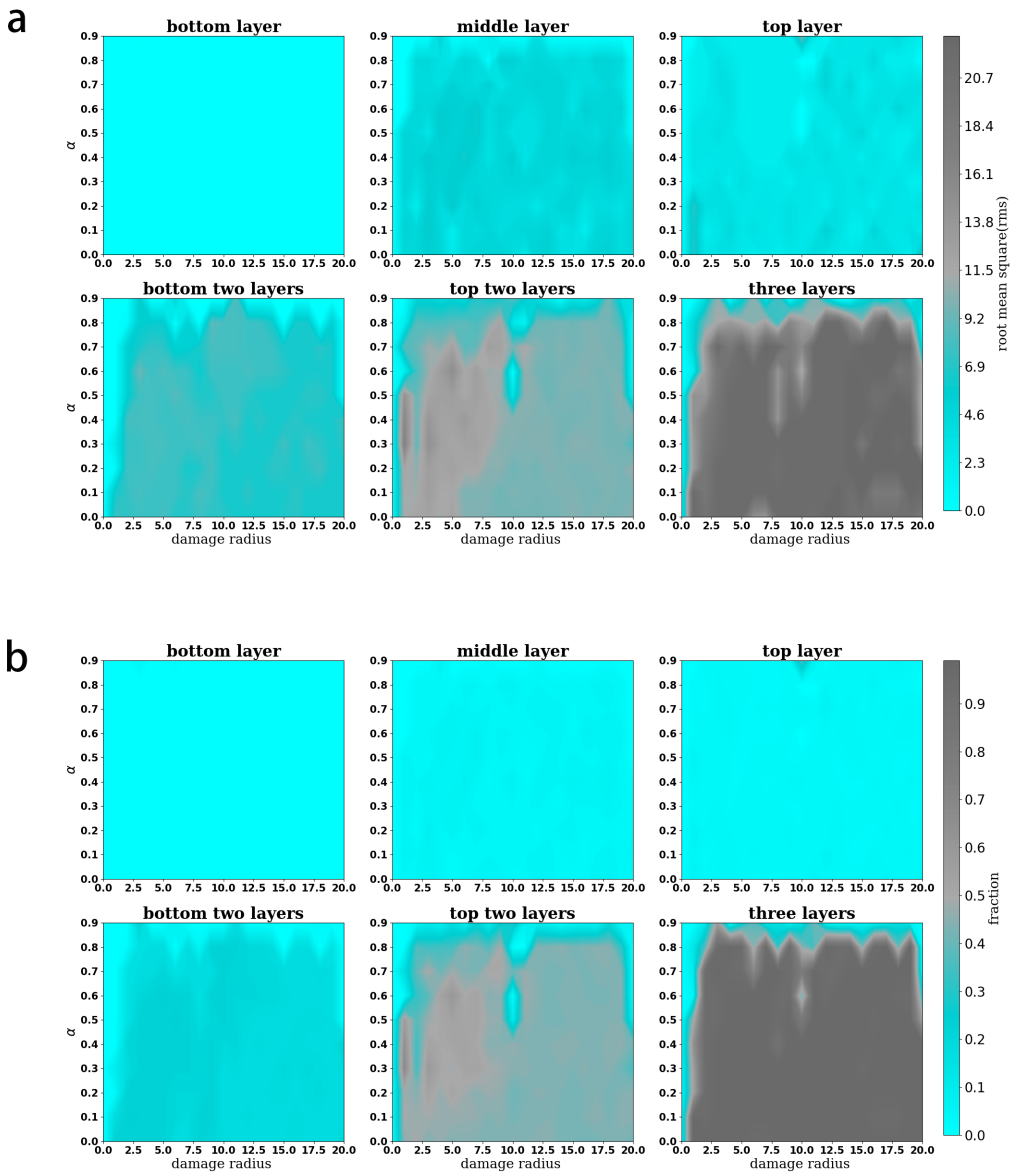

Figure 3.9. **Damage analysis over the whole variable space.** (a) Root mean square of errors (b) Error fraction in six damage cases. Damage radius ($0 < R < 20$ neurons) in horizontal axis and damage coefficient ($0.0 < \alpha < 1.0$) along the vertical. Top panels, single layer damage; Bottom panels, left, bottom two layers are damaged and the top one remain normal, middle, top two layers are damaged, right, all three layers are influenced. The colorbar are scaled into the same levels for all six cases. grid cells wavelength are (99, 70, 50) and the reduced coding range is $R_l = 40$.

top modules of grid cells determine bigger range of the locations and the following modules help to refine the resolution. The same behavior is found when we switch different grid cells wavelengths and coding range (see in Appendix B).

About the borderline in heat-map, we observe a narrow blue region shows at the right side, with big size of damage ($R > 19$) and the coefficient $\alpha \in (0.6, 1.0)$. The radius indicates that a widespread damage in the whole layer (one layer contains $N = 40$ grid cells) does not influence EGPC function if the coefficient is above a threshold. The thresholds are similar (close to 0.6) in all bottom panels of the Fig. 3.9 b.

Chapter 4

Conclusion

Part I: Neurodegenerative damage reduces firing coherence in a continuous attractor model of grid cell

We start from Burak & Fiete's attractor model of grid cells [10] to study their firing pattern on much smaller periodic neuron sheets. Smaller neuron sheets can provide good statistics on the firing pattern flow and provide reasonable results for finite and relatively short simulation times. The linearly proportional relationship between the firing pattern flow and animal's velocity input helps build a stable hexagonal lattice in the path integration map.

Applying simulated damage to the model grid cells, we observe that the firing pattern flow continues but shows bigger fluctuations (in flow speed and direction) in a longer time range. Those fluctuations accumulate errors in path integration and we observe the loss of coherent grid firing.

To identity the tolerance of grid cells to different levels of synaptic damages, we study the Bragg peaks in the Fourier Transformed pattern of position space firing fields for model grid cells, and we have shown that damage to a model grid cell layer parameterized by reduced synaptic output strength α and damage radius R leads to a predictable sequence of reduced grid cell firing symmetry from hexagonal lattice, to orthorhombic lattice, to stripes, and onto no coherent pattern (single central peak). We find that the central Bragg peak in the region with no coherent grid structure is largely unchanged for grid cells outside the damaged region, but strongly reduced

for grid cells in the damaged region. For large area damage, there is a re-entrant transition to the fully hexagonal grid structure. Grid cells can show a tolerance of certain damages. With the help of borderline in phase diagram to identify grids/no-grids region, we can control different levels of synaptic damages on grid cells and study its influence on place coding/decoding.

The modifications of the orientation of firing patterns associated with the less ordered structures should be visible in fMRI experiments which can pick up the full six fold symmetric firing pattern in the dMEC for undamaged subjects. This makes for an important tool in assessing potentially the level of synaptic damage associated with neurodegenerative diseases such as Alzheimer's, that may allow for early diagnosis and the use of small molecule aggregation inhibitor treatments such as anle138b[57, 58].

Part II: Damage impact on the grid-cell population codes for animal's locations

We aim to understand how to translate the grid periods into place coding based on the inspiration from modulo remainder coding idea [17]. The most common idea is to use the remainder of location over different grid periods for possibly effective place coding. It has the advantage of great tolerance to noise or fluctuations, and the grid population code (GPC) can code wider range of locations with fewer neurons compared with the classical population code (CPC). However, we want to know the algorithm of grid coding from the view of the neuron network, in a way that is much more realistic than the view of simplified phase vector theory. Using the readout-grid

cell networks proposed by Sreenivasan and Fiete, [16] (which still uses the modulo remainder method to associate location and grid cell firing rate), we employed the Burak & Fiete continuous attactor model for 1D case to track grid cells' firing rate as a function of animal's location. The firing rate with variable of location ($r_(x,t)$) follows the same algorithm as the path-integration map in chapter 2, and it surpasses the previous GPC using the modulo remainder phases, since $r_(x,t)$ is the immediate firing rate when grid cells are self-developing with rat's given destination and velocity. The new readout-cell network that we proposed is closer to real experiments, and it makes it possible to develop further study on impacts of damage.

Our enhanced readout-grid cell network with explicit simulation results of place-coded firing rate proves its effectiveness for accurate place coding. The stable linear-relationship between input location x and inferred location $\hat{x}$ within maximum coding range ($R_l < 500cm$) shows that the readout-grid cell network bonded simulation firing rate $r_(x,t)$ works accurately. The success in achieving effective place coding using this enhanced GPC (EGPC) made it possible for us to think about the impact of damage on grid cells in the same manner as for path integration. We have already seen the damage influence on path-integration map from chapter 2, and here we aimed to figure out what is the influence of damage on place coding. Using the center damage model with weakened synapses among grid cell, we studied different cases for various damaged layers, damaged region sizes (R) and damage coefficient (α). To identify the tolerance of grid cell layers to different levels of damages, we study the root-mean-square coding error and error points fraction. The landscape of EGPC quality heat-map of different levels of damage shows the boundary of nor-

mal/interrupted network, and a global decline of synapses weight doesn't influence the network's effectiveness when $\alpha > 0.5$ (the connection among grid cells reduces by half). We found that the damage within a single layer of grid cells doesn't destroy accurate EGPC considering that the maximum possible coding range ($R \sim N^M$) overloads the reduced coding range ($Rl < 500cm$), which require fewer layers of neurons. We noticed that the layers with bigger spacing (top layers in models, layers with deeper dorsoventral location from brain surface in experiments) show more severe disruption for the same level of damage. The fact that the fluctuations on large-spacing modules increases errors reflects the hierarchy theory of brain structures that the top panels in GPCs dominate place coding.

Chapter 5

Future work

In chapter 2 & 3 we study the continuous attractor models of grid cell network, and construct a readout-grid cell neural network that can accurately operate the grid coding of locations, and then we work on central damage model on grid cells to figure out how the possible damage (from Alzheimer's Disease) affect the path-integration map and the GPC coding qualities. What the experiments rely on is the simulations based on either 2d grid cells sheets or multiple layers of 1D gird cell lists, and to reach an effective result, we control the amounts of total grid cells within $40 \times 40 = 1600$ for 2D case, $3 \times 60 = 180$ for GPC network. We expected a much larger number of grid cells in the layers of the dMEC and experiments shows there are up to 4 or 5 modules of grid cell spacing[4], potentially up to millions of neurons. Even though we applied periodic boundary condition in all models, which can be used to represent infinite range of grid cells theoretically, we still want to know how to manipulate all models or methods in this dissertation using larger number of neurons. It may sacrifice the computational convenience but can be more realistic compared with experiments finding. We wish to see more advancement in computational ability (like clusters, parallel running setting, etc.) or better algorithm that can help speed up simulations in the future.

And for the same reason as above, we worked on coding range up to $200cm$ for both healthy and damaged GPC networks. We expected to observe the behavior when

the coding range gets bigger and even close to the GPC limitations (the theoretical limitation equals N^M where N is the number of grid cells in a layer and M is the number of layers (modules). For the 40×3 grids cell modules, the maximum coding range is $40^3 = 64000$.) As we also mentioned in chapter 3, GPC only outperforms the CPC within a reduced coding range($R_l < 500cm$), and when the coding range gets larger, the noise shows up and the inferred location has increased fluctuation around the true. How to extend the GPC coding beyond its limitation and still keep its extraordinary noise robustness is an interesting question for next stage.

As for damage model, we start from central damage model of weakening the synapses among grid cells. The periodic boundary condition helps avoid the problem of shifting location of the damage region center. But at the same time, we proposed another possible model for multiple discreet small damages on grid cell layers. How such a damage model affects the grid coding and how can we control the damage to generate a completed landscape of damage-coefficient heat-map remain unsolved. And for damaged GPC network, the weakening of neuron synapses happens among grid cells in single layer independently. So possible new situations can be the readout cell (place cell) - grid cell synapses or different layers grid cell synapses can be influenced by the lesion. As for the connection among grid cells modules, we made assumption that each layer works independently under a given spacing and no connection between adjacent layers. This helps construct GPC networks but there is no evidence to prove the irrelevance among layers of different spacing. An important question is how to fit the continuous attactor model into multiple layers case, because most current

research on grid cells attractor dynamics is for single grid spacing (the grid firing pattern wavelength).

Another surprising question about grid cells is that there exists 3D grid cells in nature. Considering we worked on 2D model of grid cells in chapter 2, and 1D model of multiple modules of grid cells in chapter 3, it is interesting to think about how to fit the GPC network into two dimensional plane, or what is the situations if grid cells can be applied into three dimensional space. The answer to the first question may be answered by adding one more axis in 2D space since we have already have an x-axis in GPC network from chapter 3. However, some details need to be considered carefully like how to project the 2D spacing into two axis, the 2D grids pattern has more characteristics (including rotation, ellipticity transformation, orientation [59]) besides the spacing wavelength. As for 3D cases, lots of findings [60–62] provide an indication possibly valid for some animals living and moving extensively in three dimensions, like for example dolphins, monkeys and even non-mammalian species (honeybees). Yet it remains unclear how brain circuits encode the animal's 3D position, but animal's (like bats) hippocampus represents 3D volumetric space by a uniform and nearly isotropic rate code[63], similar to girds pattern in space. It is an interesting brand new research field for organization of grid cells in 3D [18].

Appendix A

Supplement to Chapter 2

1. Influence of time step dt for accelerating simulation

To improve simulation effectiveness, we found the time step dt plays a big part in simulation speed. A bigger time step dt means fewer numerical simulating cycles within the same period of time. A small time step dt can improve the simulation accuracy; we find that a larger time step can also generate the hexagonal grid structure. In particular, $dt = 0.5, 1.0, 2.0ms$ can each generate a hexagonal lattice grid for a long enough animal trajectory as shown in Fig. A.1. Accordingly, we sacrifice some accuracy for better simulation speed by choosing a larger dt, which can still get sufficiently accurate results for average path integration maps.

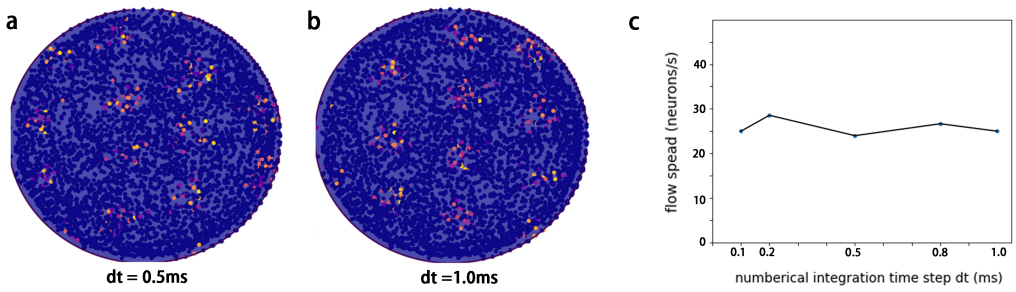

Figure A.1. **Influence of time step size dt on simulations.** (a) Average path integration map of Neuron # 800, healthy grid, dt = 0.5ms. (b) Neuron # 800, healthy grid, dt = 1.0ms. (c)different time steps $dt = 0.1ms, 0.2ms, 0.5ms, 0.8ms, 1.0ms$ don't affect the flowing speed when velocity inputs are the same ($\vec{v} = 1m/s$)

2. Explanation of flow determined by preferred direction and shifted location vectors

The grid cells can create a grid like firing pattern without the shifted location vectors $l\hat{e}_{\theta_j}$, but the inclusion of $l\hat{e}_{\theta_j}$ is the key to generate a steady firing pattern flow. The addition of $l\hat{e}_{\theta_j}$ breaks the symmetry of weight matrix W to make $W_{ij} \neq W_{ji}$ between two neurons. In Fig. A.2a,b, all the neurons have the same preferred direction $\hat{e}_{\theta_j}$ to the right, and the new weight matrix $W_{ij}(x_i - x_j - l\hat{e}_{\theta_j})$ is bigger in magnitude than $W_{ji}(x_j - x_i - l\hat{e}_{\theta_i})$ considering $l\hat{e}_{\theta_i} = l\hat{e}_{\theta_j}$. Because the weight matrix is negative, the connection along the preferred direction has bigger inhibitory affects than the connection in the opposite direction, which drives the grid-like firing pattern to move opposite to the preferred direction. When neuron groups with different preferred directions $\hat{e}_{\theta_j}$ work together equally, the symmetry of the weight matrix can be restored and that explains why there is a static firing pattern when the velocity input is zero(Fig. A.2c). When the velocity input is nonzero, it can strongly activate the neurons that share the same preferred direction, which drives the grid-like firing pattern to flow in the opposite direction to the velocity.

3. Influence of velocity input coefficient

η_0 is the coefficient that characterizes the effects of velocity inputs to the driven pattern flow, and in the paper we have taken it to be 0.10315. η_0 controls the gain from velocity to the feed-forward input $\mathbf{B}$. η_0 can be used to determine the driving force to the grid cells from the rat's velocity, and for the same velocity magnitude, a bigger η_0 can make the flow faster. The results are summarized in Fig. A.3 for

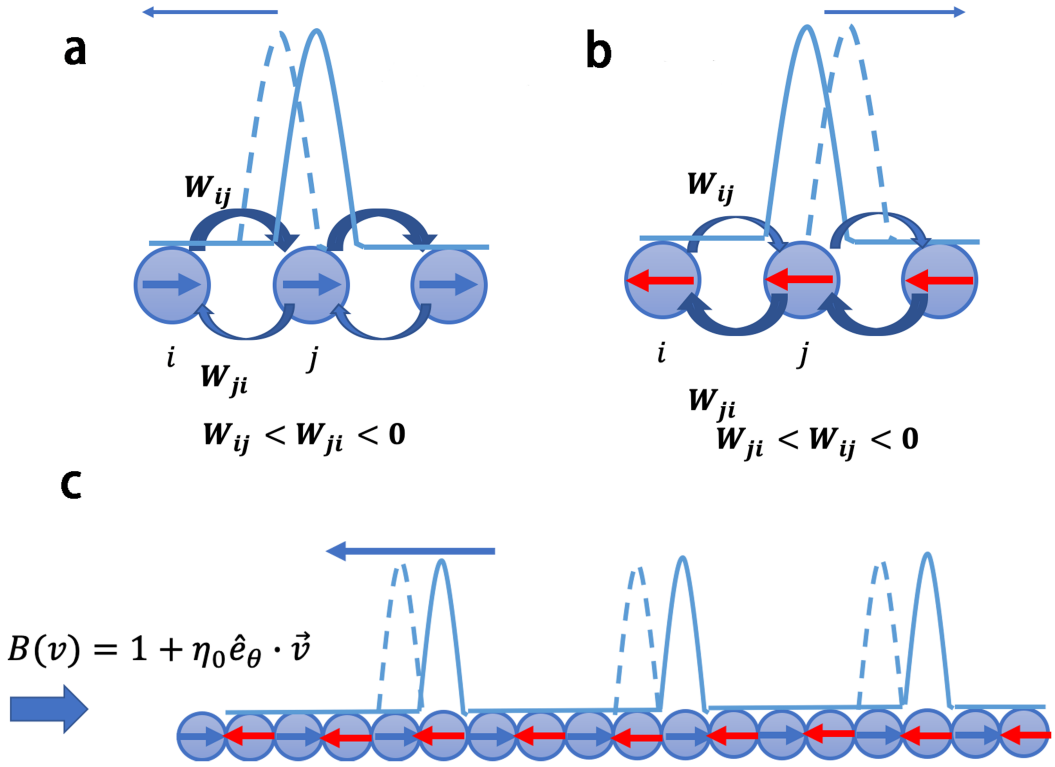

Figure A.2. **1D grid cell model with preferred direction.** (a) Neurons have preferred direction pointing to the right, breaking the symmetry of weight matrix($W_{ij} < W_{ji} < 0$), the inhibitory connection to left is bigger than that to the right, which drives the grid firing pattern to move to the left. The blue arrow indicates driving flow direction, the solid blue curve is current firing pattern and the dashed curve indicates the firing signal the next moment. (b) Neurons with preferred direction pointing to the left drive the flow pointing to the right. (c) neurons with different preferred directions work together evenly make the grid-like pattern stationary, and with non-zero velocity input pointing to the left(big blue arrow) will drive the grid to flow to the left.

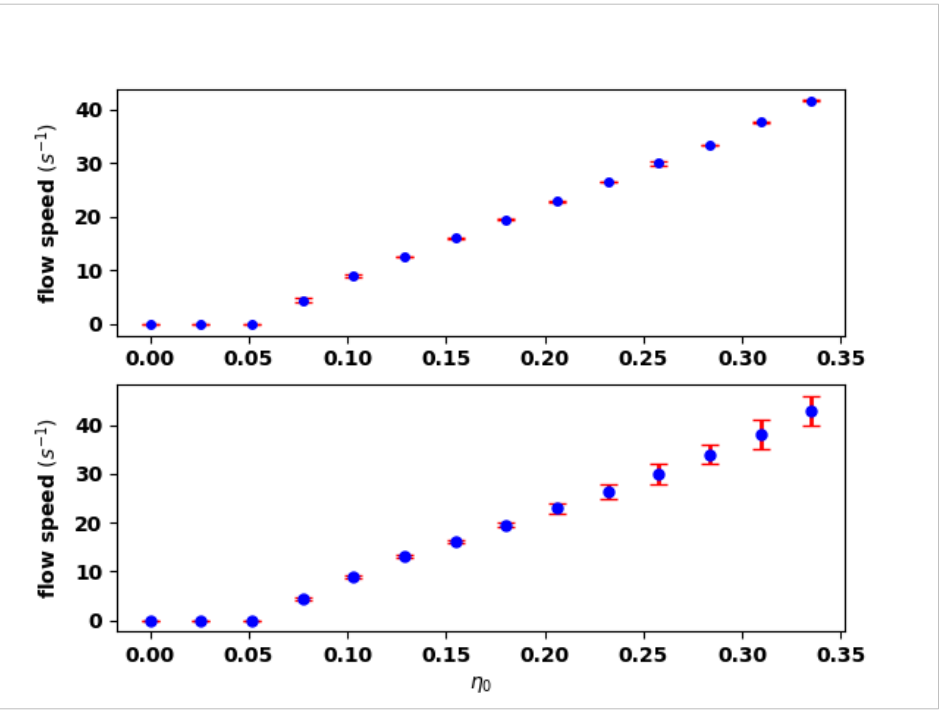

Figure A.3. **Linear relationship between flow speed and velocity input coefficient η_0.** Top: healthy neuron sheet, with input velocity taken to be 0.4 m/s. Bottom: damaged neuron sheet ($R = 4, \alpha = 0$) with the same input velocity. The red error bars are the standard deviation based upon choosing 5 trials with different random number seeds for the input noise. The first three values of flow speed are 0 in each case, indicating that the firing patterns are stationary below a critical value $\eta_0 \approx 0.05$.

both a healthy and damaged neuron sheet. This shows a linear relationship between η_0 and flow speed indistinguishable for undamaged neurons in either case. However, the larger variance for the healthy sheet with increasing η_0 shows that we want to choose ($|\eta_0 \hat{e}_{\theta_j} \cdot \vec{v}| \ll 1$) to keep the formed lattice stable. If $|\eta_0 \hat{e}_{\theta_j} \cdot \vec{v}|$ is too big ($\eta_0 > 0.35$ when $|\vec{v}| = 0.4 m/s$) then the grid-like firing pattern will disappear, and when $|\eta_0 \hat{e}_{\theta_j} \cdot \vec{v}|$ is too small ($\eta_0 \leq 0.05$), the grid-like firing pattern is frozen and not flowing any more. The same linear relationship exists for damaged neuron sheets

(Fig. A.3 bottom), with the only significant difference being that a healthy neuron outside the damaged region shows bigger variance of the flow velocities than for the undamaged sheet.

4. Mean Field Analysis to explain triangular grid

The firing rate equations for Burak and Fiete are:

$$\tau \frac{ds_i}{dt} = -s_i + f\left(\sum W_{ij} \cdot s_i + B_i\right) \tag{A.1}$$

where:

$$W_{ij} = e^{-\gamma|\vec{x_i}-\vec{x_j}|} - e^{-\beta|\vec{x_i}-\vec{x_j}|} \tag{A.2}$$

with $w_{ij} < 0$ uniformly and $s_i > 0, B = 1$. There is no region of s_i space where the argument of the rectification in $(C1)$ is negative hence $(C1)$ is always in the linear regime.

The fixed point is set by the condition

$$\frac{ds_i}{dt} = 0 \tag{A.3}$$

with $s_i = \sum W_{ij} \cdot s_i + B$ which can be viewed as the solution arising from minimizing the "cost function"

$$C(s_i) = \frac{1}{2}\sum {s_i}^2 - \sum B \cdot s_i - \frac{1}{2} s_i W_{ij} s_j \quad . \tag{A.4}$$

Fourier transformation of the firing rates is given by

$$s_i = \frac{1}{\sqrt{N}} \sum \widetilde{s}(\widetilde{q}) e^{-i \cdot \widetilde{q} \cdot r_i} \tag{A.5}$$

$\vec{r}_i$ is the neuron position in $N \times N$ sheets; $\vec{r}_i + N\hat{x} = \vec{r}_i + N\hat{y} = \vec{r}_i$. $\widetilde{q} \subset [q_x, q_y], -\frac{\pi(N-1)}{N} \leq q_\alpha \leq \pi, \alpha = x, y.$ where

$$\widetilde{W}(\widetilde{q}) = \frac{\pi}{\gamma} e^{-\frac{q^2}{4\gamma}} - \frac{\pi}{\beta} e^{-\frac{q^2}{4\beta}} \tag{A.6}$$

With $\widetilde{W}(\widetilde{q}) > 1$, an instability at finite $\widetilde{q}$ is possible. $\widetilde{W}(0) = \frac{\pi}{\gamma} - \frac{\pi}{\beta}$, and $\widetilde{W}(\widetilde{q})$ is maximum when $\widetilde{q_0} = 2\sqrt{2(\frac{\beta\gamma}{\gamma-\beta}) \ln(\frac{\gamma}{\beta})}$.

We can assume different solutions of the form

$$s_i(\vec{r}) = a_i[1 + b_i \sum f_i(\widetilde{q_k} \cdot \vec{r})] \tag{A.7}$$

where $|\widetilde{q_k}| = q_0$, and there are constraints:

(1) $1 + b_i \sum f_i(\widetilde{q_k} \cdot \vec{r}) \geq 0$

(2) $f_i(\widetilde{q_k} \cdot \vec{r})$ must be periodic.

Examples are:

(1) $s_0(\vec{r}) = a_0$, uniformly.

(2) $s_1(\vec{r}) = a_1[1 + \cos(q_0 x)]$, periodical along x direction.

(3) $s_2(\vec{r}) = a_2[1 + \frac{1}{2}\cos(q_0 x) + \frac{1}{2}\cos(q_0 x)]$, orthorhombic grid.

(4) $s_3(\vec{r}) = a_3[1 + \frac{2}{3}\cos(\vec{q}_1\vec{r}) + \frac{2}{3}\cos(\vec{q}_2\vec{r}) + \frac{2}{3}\cos(\vec{q}_3\vec{r})]$, triangular grid.

where $\vec{q}_1 = q_0(1, 0)$, $\vec{q}_2 = q_0(-\frac{1}{2}, \frac{\sqrt{3}}{2})$, $\vec{q}_3 = q_0((-\frac{1}{2}, -\frac{\sqrt{3}}{2})$.

Their Fourier Transforms are

(1) $\widetilde{s_0}(\widetilde{q}) = a_0\delta_{\widetilde{q},0}$

(2) $\widetilde{s_1}(\widetilde{q}) = a_1[\delta_{\widetilde{q},0} + \frac{1}{2}(\delta_{\widetilde{q},q_0x} + \delta_{\widetilde{q},-q_0x})]$

(3) $\widetilde{s_2}(\widetilde{q}) = a_2[\delta_{\widetilde{q},0} + \frac{1}{4}(\delta_{\widetilde{q},q_0x} + \delta_{\widetilde{q},-q_0x} + \delta_{\widetilde{q},q_0y} + \delta_{\widetilde{q},-q_0y})]$

(4) $\widetilde{s_3}(\widetilde{q}) = a_3[\delta_{\widetilde{q},0} + \frac{1}{3}(\delta_{\vec{q}_1\cdot\vec{r}} + \delta_{-\vec{q}_1\cdot\vec{r}} + \delta_{\vec{q}_2\cdot\vec{r}} + \delta_{-\vec{q}_2\cdot\vec{r}} + \delta_{\vec{q}_3\cdot\vec{r}} + \delta_{-\vec{q}_3\cdot\vec{r}})]$

Substituting these in the cost function yields the results

$$C[\widetilde{S}_{\widetilde{q}}] = \frac{1}{2}\sum_{\widetilde{q}} |\widetilde{s}(\widetilde{q})|^2[1 - \widetilde{W}(\widetilde{q})] - \sqrt{N}B\widetilde{s}(\widetilde{q} = 0) \tag{A.8}$$

(1) $C_0 = -\sqrt{N}Ba_0 + \frac{{a_0}^2}{2}[1 - \widetilde{W}(0)]$

(2) $C_1 = -\sqrt{N}Ba_1 + \frac{{a_1}^2}{2}\{[1 - \widetilde{W}(0)] + \frac{1}{2}[1 - \widetilde{W}(q_0)]\}$

(3) $C_2 = -\sqrt{N}Ba_2 + \frac{{a_2}^2}{2}\{[1 - \widetilde{W}(0)] + \frac{1}{4}[1 - \widetilde{W}(q_0)]\}$

(4) $C_3 = -\sqrt{N}Ba_3 + \frac{{a_3}^2}{2}\{[1 - \widetilde{W}(0)] + \frac{2}{3}[1 - \widetilde{W}(q_0)]\}$

We can summarize these results as:

$$C_i = -\sqrt{N}Ba_i + \frac{{a_i}^2}{2}\{[1 - \widetilde{W}(0)] + \sigma_i[1 - \widetilde{W}(q_0)]\} \tag{A.9}$$

Introducing

$$\rho_i = [1 - \widetilde{W}(0)] + \sigma_i[1 - \widetilde{W}(q_0)] \tag{A.10}$$

Equation (C9) can be changed into:

$$C_i = \frac{\rho_i}{2}\left(a_i - \frac{\sqrt{N}B}{\rho_i}\right)^2 - \frac{NB^2}{2\rho_i} \tag{A.11}$$

$$C_{i,\min} = -\frac{NB^2}{2\rho_i} \quad \text{when} \quad a_i = \frac{\sqrt{N}B}{\rho_i} \tag{A.12}$$

For a 40×40 neuron sheet with $a = 1$, $N = 1600$, $B = 1$, $\gamma = 6.7 \times \beta$, $\beta = \frac{3}{64}$; We have $\widetilde{q}_0 = 0.916$, and $\widetilde{W}(0) = -57.02$, $\widetilde{W}(\widetilde{q}_0) = 4.37$.

(1) $C_{0,\min} = -13.79, \quad a_0 = 0.689$

(2) $C_{1,\min} = -14.20, \quad a_1 = 0.71$

(3) $C_{2,\min} = -13.99, \quad a_2 = 0.6995$

(4) $C_{3,\min} = -14.34, \quad a_3 = 0.7172$

Notice that the hexagonal grid shows the lowest cost, indicating it is more stable than grid structures.

5. Aperiodic boundary conditions

the feed-forward input to neuron i is:

$$B_i(x) = A_i(x)(1 + \eta_0 \cdot \hat{e}_{\theta_i} \cdot \vec{v}) \tag{A.13}$$

$A_i(x)$ is called the *envelope function* which helps to modulate the strength of the input to the neurons.

$$A(\vec{x}) = \begin{cases} 1 & |\vec{x}| < R - \Delta r \\ exp[-a_0(\frac{|\vec{x}|-R+\Delta r}{\Delta r})^2] & R - \Delta r \leq |\vec{x}| \leq R \end{cases} \tag{A.14}$$

$R = 20$ is the radius of the 40×40 network and $a_0 = 4$. Δr determines the range of radius over which input tapering occurs, the larger Δr, the more gradual the tapering. In all aperiodic simulations, $\Delta r = R$. [Burak. & Fiete.]

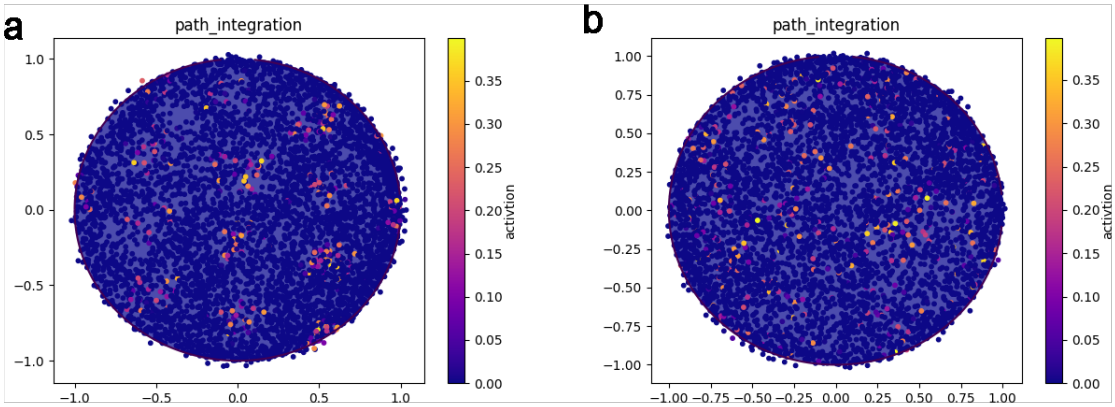

Figure A.4. **Longer path integration maps of healthy and damaged neuron sheets.** a, Healthy neuron sheets, 500s path integration map of neuron #800, b, Damaged neuron sheets ($\alpha = 0.8, R = 7$), 500s path integration map of neuron #800.

6. Influence of increasing length for path integration map

To check the what happened when we use longer paths for simulation, we ran for 5× longer trajectories (500s) and present the result in Fig. A.4. The healthy neuron sheets can generate a grid-like pattern and the damaged one loses its grid. Comparing with the method (in the main paper) of using the average of five independent shorter trajectories (100s), the results of those longer runs are similar to those of the shorter ones, so that an increasing length doesn't destroy or enhance the grid-like pattern in a healthy neuron sheet. We can say the path integration map is still stable within a long time range (up to 500s), and for the same damage situation ($\alpha = 0.8, R = 7$), we find similar loss of grid firing as for the shorter time runs. It is safe to conclude that the grid pattern loss is not eliminated by a longer path integration but the defects. Meanwhile, using an average of independent trajectories is more effective because we can do parallel simulations at the same time.

Appendix B

Supplement to Chapter 3

1. Place coded firing rate $r_{\alpha j}(x,t)$ from 1D Burak & Fiete's model

The original Burak & Fiete's model can accurately integrate velocity inputs over a certain range to simulate rat's path integration map in a circular enclosure. What we need here in GPC network is the accurate firing rates of grid cells when animal is at one target location. We want to explain how to bond the velocity input with animal's current location here.

Inherited from Chapter 2, we assume that the linear relationship between firing rate flow speed and animal's moving velocity always exists for healthy gird cells network. That is:

$$\text{flowing speed} = K \cdot |\vec{\mathbf{v}}| \tag{B.15}$$

The linear relationship above make sure that the firing rate change is only the function of animal's displacement vector, regardless of animal's moving velocity or the time it takes to reach the destination. Using a simple toy model in Fig. A.5: there is a 1D list of 20 grid cells and firing rate is shown above the neurons. Suppose at the beginning time, the firing peaks is at the first one in the neuron list, and the wavelength of the periodicity is 10 neurons, and we can assume $K = 20\ neurons/m$ in the model. We have initial states that neurons 1^{th}, 11^{th} are active (Fig. A.5a).

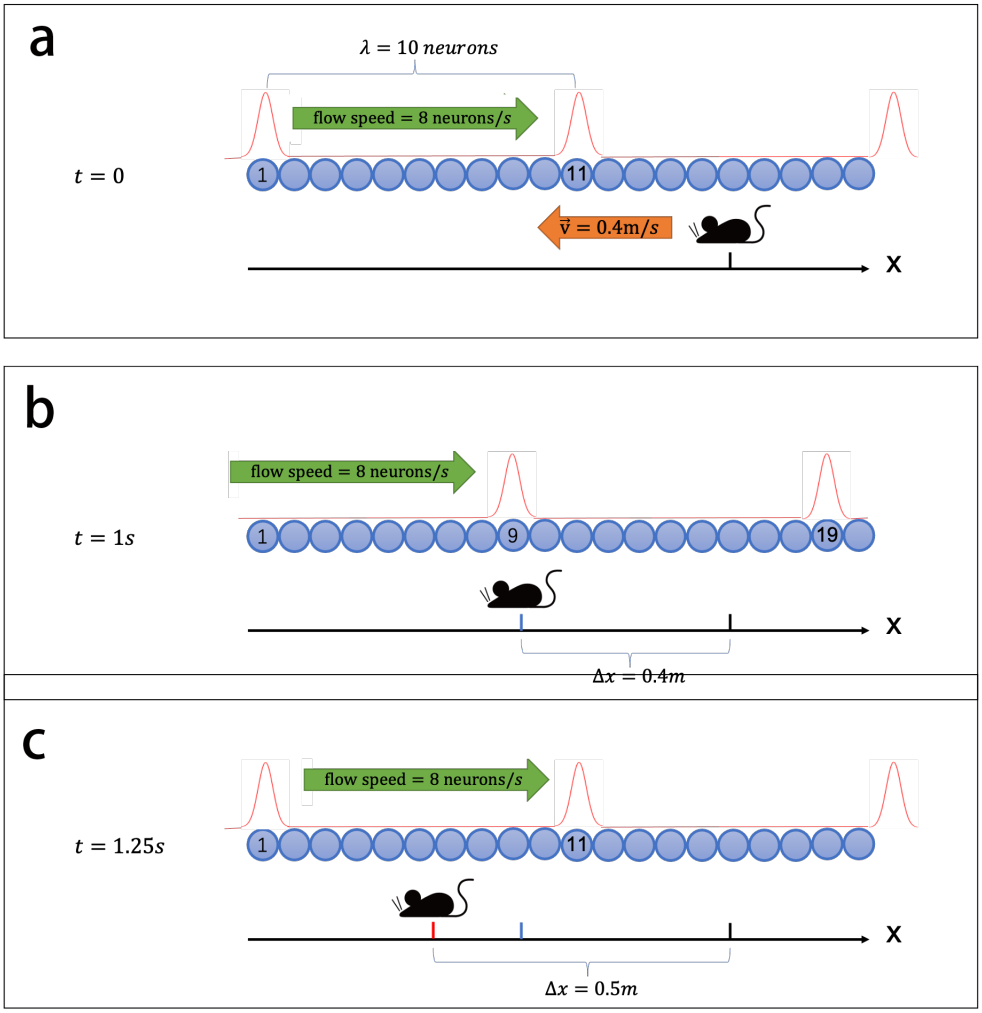

Figure A.5. **Linear model of rat's displacement in real space and firing rate flow moving.** (a) Blue spheres represents 1D list of 20 gird cells with number indicating index, the spacing between peaks is the wavelength of the firing pattern: $\lambda = 10$ neurons. The rat is moving along horizontal axis towards left with a constant velocity $|\vec{v}| = 0.4\ m/s$. The initial location is shown in black. (b) $t = 1s$, the rat moves $0.4m$ to new location in blue. The firing peaks flow to the right direction and now 9^{th}, 19^{th} neurons are active. (c) $t = 1.25s$, the rat moves $0.5m$ to destination in red. 1^{th}, 11^{th} neurons fire again as the initial states.

Thus, when rat starts to move at a constant velocity pointing to the left side $\vec{v} = 0.4\ m/s$, it indicates the firing rate flow moves to the left side with flow speed $= 20 \times 0.4 = 8\ neurons/s$. And it takes $1s$ to reach new position $\Delta x = 0.4m$ while the initial peaks are shifted to the right by 8 neurons. Now the 9^{th}, 19^{th} neuron are active (Fig. A.5b). To make the firing rates back to initial states (1^{th}, 11^{th} activates), we need $0.25s$ more and the new displacement is $\Delta x = 0.5m$ and the firing peaks shifted by 10 neurons, which equals the periodicity (Fig. A.5c).

This 1D model proves that the linear relationship between flow speed and velocity input tightly bind the firing rate change with animal's displacement vectors. Like in above example, the firing rates peaks are shifted by 10 neurons when the rat moves every $0.5m$. Thus, we can figure out what is the place coded grid cell firing rates $r_{\alpha j}(x, t)$ in the following way:

(1) Choose an initial state of periodic firing pattern on grid cell layers, which can be the first states right after the annealing process (see in section 2.2.1). Name it as initial firing rates: $r_{\alpha j}(x = x_i, t = 0)$ with x_i to be the initial position of the rat.

(2) Set the target location be x_t, so $r_{\alpha j}(x = x_t, t)$ is the firing rate of grid cells when animal moves to location x_t. Set average moving velocity of rats be $|\vec{v}|$, and then:

$$r_{\alpha j}(x_t, t) \quad = \quad r_{\alpha j}(x, t = x_t/|\vec{v}|) \tag{B.16}$$

We get the place coded firing rate at x_t after the initial states develops for a period time of $t = x_t/|\vec{v}|$.

In the above example where $|\vec{v}| = 0.4\ m/s$, if the target location is $x_t = 0.4m$, the states after a period of time $t = 1000ms$ can provide us the place coded firing rate:

$$r_{\alpha j}(x = 0.4m) = \begin{cases} 1 & (j = 9, 19) \\ 0 & (otherwise) \end{cases} \tag{B.17}$$

with 1 indicates neuron fires, and 0 indicates neuron mutes. And the simulation time increases with the growing coding range R_l.

2. Landscape map with different grid periods λ and reduced coding range R_l

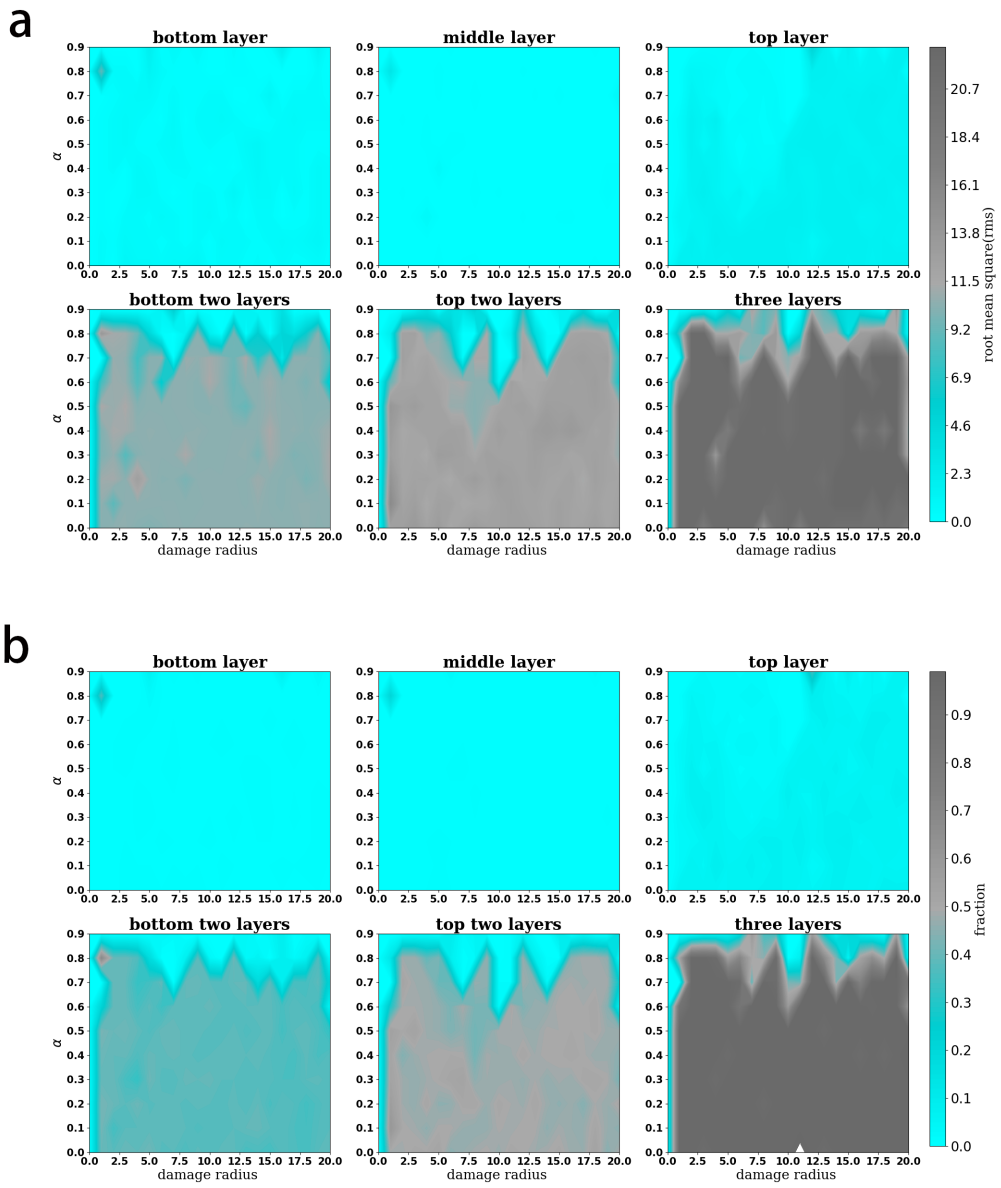

Figure A.6. **Damage analysis over the whole variable space. Gird cells wavelength are (90, 63, 45) and the reduced coding range is $R_l = 40$.** (a) Root mean square of errors (b) Error fraction in six damage cases. Damage radius ($0 < R < 20$ neurons) in horizontal axis and damage coefficient ($0.0 < \alpha < 1.0$) along the vertical. Top panels, single layer damage; Bottom panels, left, bottom two layers are damaged and the top one remain normal, middle, top two layers are damaged, right, all three layers are influenced. The colorbar are scaled into the same levels for all six cases.

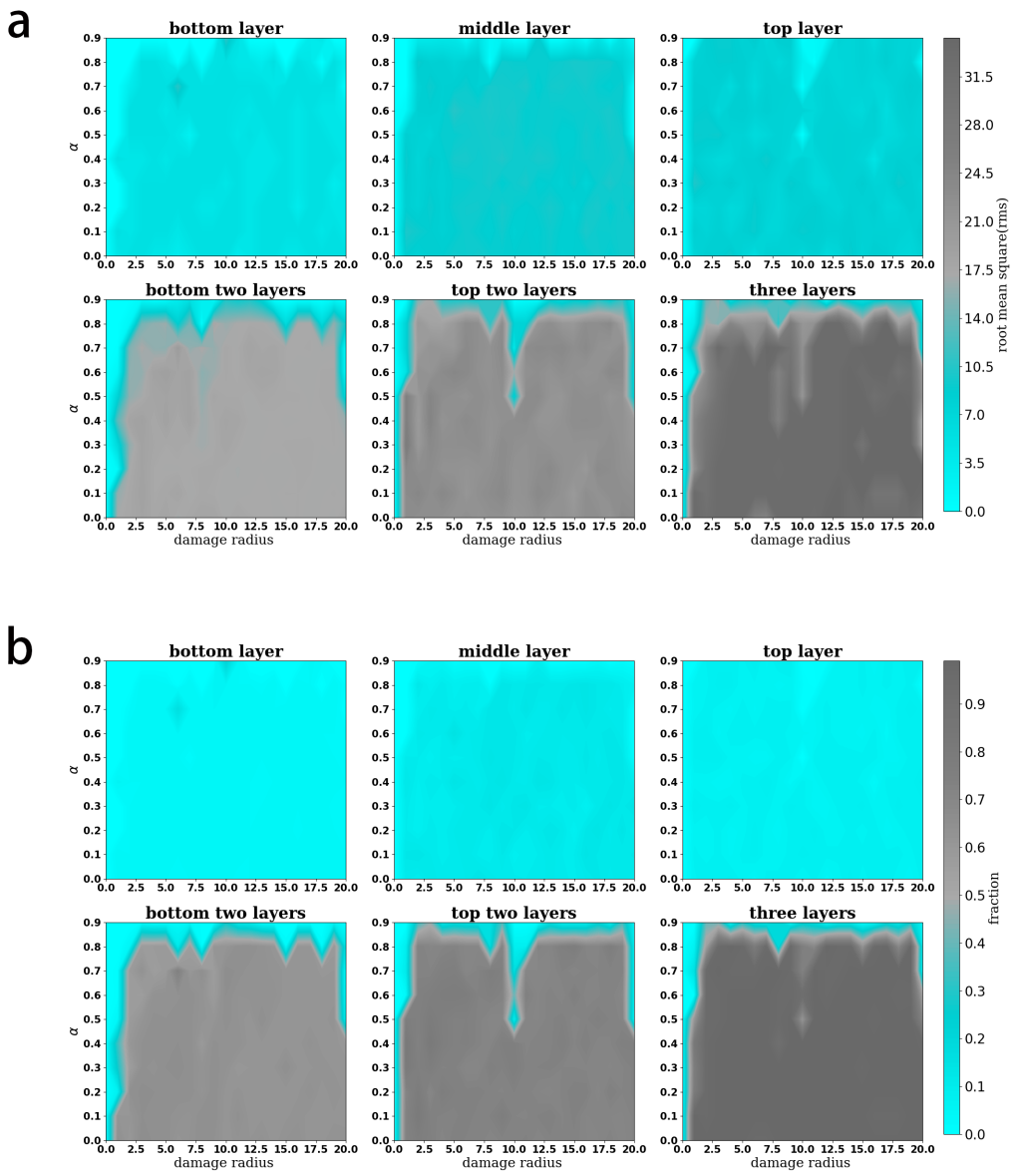

Figure A.7. **Damage analysis over the whole variable space. Gird cells wavelength are (99, 70, 50) and the reduced coding range is $R_l = 60$.** (a) Root mean square of errors (b) Error fraction in six damage cases. Damage radius ($0 < R < 20$ neurons) in horizontal axis and damage coefficient ($0.0 < \alpha < 1.0$) along the vertical. Top panels, single layer damage; Bottom panels, left, bottom two layers are damaged and the top one remain normal, middle, top two layers are damaged, right, all three layers are influenced. The colorbar are scaled into the same levels for all six cases.

Bibliography

1. Solstad, T., Boccara, C. N., Kropff, E., Moser, M.-B. & Moser, E. I. Representation of geometric borders in the entorhinal cortex. *Science* **322,** 1865–1868 (2008).

2. Hafting, T., Fyhn, M., Molden, S., Moser, M.-B. & Moser, E. I. Microstructure of a spatial map in the entorhinal cortex. *Nature* **436,** 801–806 (2005).

3. Fyhn, M., Hafting, T., Treves, A., Moser, M.-B. & Moser, E. I. Hippocampal remapping and grid realignment in entorhinal cortex. *Nature* **446,** 190–194 (2007).

4. McNaughton, B. L., Battaglia, F. P., Jensen, O., Moser, E. I. & Moser, M.-B. Path integration and the neural basis of the'cognitive map'. *Nature Reviews Neuroscience* **7,** 663–678 (2006).

5. Brun, V. H. *et al.* Progressive increase in grid scale from dorsal to ventral medial entorhinal cortex. *Hippocampus* **18,** 1200–1212 (2008).

6. Stensola, H. *et al.* The entorhinal grid map is discretized. *Nature* **492,** 72–78 (2012).

7. Urdapilleta, E., Si, B. & Treves, A. S elforganization of modular activity of grid cells. *Hippocampus* **27,** 1204–1213 (2017).

8. Wei, X.-X., Prentice, J. & Balasubramanian, V. The sense of place: grid cells in the brain and the transcendental number e. *arXiv preprint* (2013).

9. Yoon, K. *et al.* Specific evidence of low-dimensional continuous attractor dynamics in grid cells. *Nature Neuroscience* **16,** 1077–1084 (2013).

10. Burak, Y. & Fiete, I. R. Accurate path integration in continuous attractor network models of grid cells. *PLoS Comput Biol* **5,** e1000291 (2009).

11. Shipston-Sharman, O., Solanka, L. & Nolan, M. F. Continuous attractor network models of grid cell firing based on excitatory–inhibitory interactions. *The Journal of Physiology* **594,** 6547–6557 (2016).

12. Burgess, N., Barry, C. & O'Keefe, J. An oscillatory interference model of grid cell firing. *Hippocampus* **17,** 801–812 (2007).

13. Burgess, N. Grid cells and theta as oscillatory interference: theory and predictions. *Hippocampus* **18,** 1157–1174 (2008).

14. Jeewajee, A., Barry, C., O'Keefe, J. & Burgess, N. Grid cells and theta as oscillatory interference: electrophysiological data from freely moving rats. *Hippocampus* **18,** 1175–1185 (2008).

15. Bush, D. & Burgess, N. A hybrid oscillatory interference/continuous attractor network model of grid cell firing. *Journal of Neuroscience* **34,** 5065–5079 (2014).

16. Sreenivasan, S. & Fiete, I. Grid cells generate an analog error-correcting code for singularly precise neural computation. *Nature Neuroscience* **14,** 1330–U154. ISSN: 1097-6256 (2011).

17. Fiete, I. R., Burak, Y. & Brookings, T. What grid cells convey about rat location. *Journal of Neuroscience* **28,** 6858–6871 (2008).

18. Stella, F. & Treves, A. The self-organization of grid cells in 3D. *Elife* **4,** e05913 (2015).

19. O'Keefe, J. & Nadel, L. *The Hippocampus as a Cognitive map* (Oxford: Clarendon Press, 1978).

20. Muir, G. M. & Bilkey, D. K. Instability in the place field location of hippocampal place cells after lesions centered on the perirhinal cortex. *Journal of Neuroscience* **21,** 4016–4025 (2001).

21. Chen, L. L., Lin, L.-H., Green, E. J., Barnes, C. A. & McNaughton, B. L. Head-direction cells in the rat posterior cortex. *Experimental Brain Research* **101,** 8–23 (1994).

22. Taube, J. S., Muller, R. U. & Ranck, J. B. Head-direction cells recorded from the postsubiculum in freely moving rats. I. Description and quantitative analysis. *Journal of Neuroscience* **10,** 420–435 (1990).

23. Seelig, J. D. & Jayaraman, V. Neural dynamics for landmark orientation and angular path integration. *Nature* **521,** 186–191 (2015).

24. Doeller, C. F., Barry, C. & Burgess, N. Evidence for grid cells in a human memory network. *Nature* (2010).

25. Constantinescu, A. O., O'Reilly, J. X. & Behrens, T. E. J. Organizing conceptual knowledge in humans with a gridlike code. *Science* **352,** 1464–1468. ISSN: 0036-8075 (2016).

26. Garvert, M. M., Dolan, R. J. & Behrens, T. E. J. A map of abstract relational knowledge in the human hippocampal-entorhinal cortex. *Elife* **6.** ISSN: 2050-084X (2017).

27. Nau, M., Schroder, T. N., Bellmund, J. L. S. & Doeller, C. F. Hexadirectional coding of visual space in human entorhinal cortex. *Nature Neuroscience.* ISSN: 1097-6256 (2018).

28. Mudher, A. & Lovestone, S. Alzheimer's disease–do tauists and baptists finally shake hands? *Trends in Neurosciences* **25,** 22–26 (2002).

29. Goedert, M., Spillantini, M. & Crowther, R. Tau proteins and neurofibrillary degeneration. *Brain pathology* **1,** 279–286 (1991).

30. Chun, W. & Johnson, G. The role of tau phosphorylation and cleavage in neuronal cell death. *Frontiers in Bioscience: A Journal and Virtual Library* **12,** 733 (2007).

31. Wilesmith, J. W., Wells, G., Cranwell, M. P. & Ryan, J. Bovine spongiform encephalopathy: epidemiological studies. *The Veterinary Record* **123,** 638 (1988).

32. Casalone, C. & Hope, J. in *Handbook of Clinical Neurology* 121–134 (Elsevier, 2018).

33. Darwin, C. *Origin of Certain Instincts* 1873.

34. De Strooper, B. & Karran, E. The Cellular Phase of Alzheimer's Disease. *Cell* **164,** 603–615. ISSN: 0092-8674 (2016).

35. Cline, E. N., Bicca, M. A., Viola, K. L. & Klein, W. L. The Amyloid-beta Oligomer Hypothesis: Beginning of the Third Decade. *Journal of Alzheimers Disease* **64,** S567–S610. ISSN: 1387-2877 (2018).

36. Van Hoesen, G. W., Hyman, B. T. & Damasio, A. R. Entorhinal cortex pathology in Alzheimer's disease. *Hippocampus* **1,** 1–8. ISSN: 1050-9631 (1991).

37. Kunz, L. *et al.* Reduced grid-cell-like representations in adults at genetic risk for Alzheimer's disease. *Science* **350,** 430–433. ISSN: 0036-8075 (2015).

38. Stangl, M. *et al.* Compromised Grid-Cell-like Representations in Old Age as a Key Mechanism to Explain Age-Related Navigational Deficits. *Current Biology.* ISSN: 0960-9822 (2018).

39. Zempel, H. *et al.* Amyloid-beta oligomers induce synaptic damage via Tau-dependent microtubule severing by TTLL6 and spastin. *Embo Journal* **32,** 2920–2937. ISSN: 0261-4189 (2013).

40. Chen, Y. *et al.* Expression of human Tau40 in the medial entorhinal cortex impairs synaptic plasticity and associated cognitive functions in mice. *Biochemical*

and Biophysical Research Communications **496,** 1006–1012. ISSN: 0006-291X (2018).

41. Fu, H. *et al.* Tau Pathology Induces Excitatory Neuron Loss, Grid Cell Dysfunction, and Spatial Memory Deficits Reminiscent of Early Alzheimer's Disease. *Neuron.* ISSN: 0896-6273 (2017).

42. Yang, X. *et al.* A novel mechanism of memory loss in Alzheimer's disease mice via the degeneration of entorhinal-CA1 synapses. *Molecular Psychiatry* **23,** 199–210. ISSN: 1359-4184 (2018).

43. Couey, J. J. *et al.* Recurrent inhibitory circuitry as a mechanism for grid formation. *Nature Neuroscience* **16,** 318–324. ISSN: 1097-6256 (2013).

44. Dayan, P., Abbott, L. F., *et al.* Theoretical neuroscience: computational and mathematical modeling of neural systems. *Journal of Cognitive Neuroscience* **15,** 154–155 (2003).

45. West, M. J. & Slomianka, L. Total number of neurons in the layers of the human entorhinal cortex. *Hippocampus* **8,** 69–82 (1998).

46. Hall, G. F. & Patuto, B. A. Is tau ready for admission to the prion club? *Prion* **6,** 223–233. ISSN: 1933-6896 (2012).

47. Samsonovich, A. V. & Ascoli, G. A. A simple neural network model of the hippocampus suggesting its pathfinding role in episodic memory retrieval. *Learning & Memory* **12,** 193–208 (2005).

48. Balasubramanian, V. Heterogeneity and efficiency in the brain. *Proceedings of the IEEE* **103,** 1346–1358 (2015).

49. Grieves, R. M. *et al.* The place-cell representation of volumetric space in rats. *Nature Communications* **11,** 1–13 (2020).

50. Diba, K. & Buzsáki, G. Forward and reverse hippocampal place-cell sequences during ripples. *Nature Neuroscience* **10,** 1241–1242 (2007).

51. Brun, V. H. *et al.* Impaired spatial representation in CA1 after lesion of direct input from entorhinal cortex. *Neuron* **57,** 290–302 (2008).

52. Pouget, A., Dayan, P. & Zemel, R. Information processing with population codes. *Nature Reviews Neuroscience* **1,** 125–132 (2000).

53. Sanger, T. D. Neural population codes. *Current Opinion in Neurobiology* **13,** 238–249 (2003).

54. Aoki, C. & Siekevitz, P. Plasticity in brain development. *Scientific American* **259,** 56 (1988).

55. Wilson, M. A. & McNaughton, B. L. Dynamics of the hippocampal ensemble code for space. *Science* **261,** 1055–1058 (1993).

56. MacKay, D. J. & Mac Kay, D. J. *Information theory, inference and learning algorithms* (Cambridge university press, 2003).

57. Antonschmidt, L. *et al.* Protein-Drug Interactions in the Membrane: The Small Molecule Anle138b and its Binding to alpha-Synuclein Oligomers. *Biophysical Journal* **116,** 352A–352A (2019).

58. Antonschmidt, L. *et al.* The Small Molecule anle138b Shows Interaction with alpha-Synuclein Oligomers in Phospholipid Membranes. *Biophysical Journal* **114,** 560A–560A. ISSN: 0006-3495 (2018).

59. Sanzeni, A., Balasubramanian, V., Tiana, G. & Vergassola, M. Complete coverage of space favors modularity of the grid system in the brain. *Physical Review E* **94.** ISSN: 2470-0045 (2016).

60. Ulanovsky, N. & Moss, C. F. Dynamics of hippocampal spatial representation in echolocating bats. *Hippocampus* **21,** 150–161 (2011).

61. Yartsev, M. M., Witter, M. P. & Ulanovsky, N. Grid cells without theta oscillations in the entorhinal cortex of bats. *Nature* **479,** 103–107 (2011).

62. Dacke, M. & Srinivasan, M. V. Honeybee navigation: distance estimation in the third dimension. *Journal of Experimental Biology* **210,** 845–853 (2007).

63. Yartsev, M. M. & Ulanovsky, N. Representation of three-dimensional space in the hippocampus of flying bats. *Science* **340,** 367–372 (2013).